NASA TECHNICAL NOTE

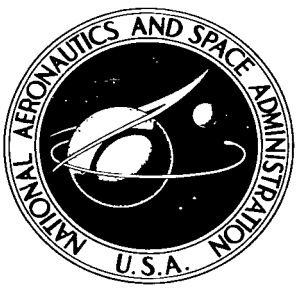

NASA TN D-4012

CORONAL PHOTOGRAPHS, ISOPHOTES, AND A FLASH SPECTRUM FROM THE SOLAR ECLIPSE OF MAY 30, 1965

by Sheldon M. Smith, Milton E. Henderson, and Ray A. Torrey

Ames Research Center
Moffett Field, Calif.

NATIONAL AERONAUTICS AND SPACE ADMINISTRATION • WASHINGTON, D. C. • JUNE 1967

NASA TN D-4012

CORONAL PHOTOGRAPHS, ISOPHOTES, AND A FLASH SPECTRUM FROM THE SOLAR ECLIPSE OF MAY 30, 1965

By Sheldon M. Smith, Milton E. Henderson, and Ray A. Torrey

Ames Research Center
Moffett Field, Calif.

NATIONAL AERONAUTICS AND SPACE ADMINISTRATION

For sale by the Clearinghouse for Federal Scientific and Technical Information
Springfield, Virginia 22151 – CFSTI price $3.00

CORONAL PHOTOGRAPHS, ISOPHOTES, AND A FLASH SPECTRUM FROM THE SOLAR ECLIPSE OF MAY 30, 1965

By Sheldon M. Smith, Milton E. Henderson, and Ray A. Torrey

Ames Research Center

SUMMARY

This paper describes the instrumentation used to measure photographically the distribution of coronal brightness from the CV-990 aircraft at an altitude of 38,000 feet during the eclipse of May 30, 1965. The initial data and photographs are presented and the photometric accuracy of the data is analyzed. At the 3-5 arcsec level of spatial resolution, no optical evidence of aircraft boundary-layer turbulence or window deformation was observed. The most difficult problem associated with coronal observation from an aircraft is stabilization of the line of sight for long exposures. The flash spectrum produced accurate positional evidence of 8 prominences on or near the east limb in addition to recording some 50 chromospheric and 2 coronal emission lines. A probable upper limit for instrumental scattering during a natural eclipse was established at about 10 percent of the total coronal brightness. The extremely good agreement of the absolutely calibrated isophotes presented herein with the polar coronal brightnesses measured by previous observers places the photometric error at less than ±18 percent for the inner corona and less than ±13 percent beyond $2R_{\odot}$. An error by a factor of about 1.8 has apparently been found in the absolute brightnesses given for this eclipse by Professor Waldmeier. The photometrically uniform south polar corona has been shown to extend to position angles $\pm 55^{\circ}$ from the polar axis. Within 1.8 $R_{\odot}$ the polar regions are about one-third as bright as a major streamer. Detailed structure of the inner and mid corona is shown on photographs obtained with a radial transmission filter. The manner in which a young center of activity on the solar surface disrupts the form of the quiet corona can be seen in these photographs by comparing the structure over the permanent condensation with that on the opposite limb. Photometric analysis of the photographs taken through a polarizer should produce electron densities for the larger structures in the photographs.

INTRODUCTION

The structure of the spatial distribution of electrons in the solar corona is important because it provides information concerning the hydromagnetic interaction of coronal plasma with the outer magnetic fields of the Sun. This interaction is of interest for three types of study. By itself, it is of physical interest because it occurs in the 2-4 million degree Kelvin, low-density coronal environment that cannot be duplicated in laboratories. For

studies of the solar wind, this interaction is of prime importance because it must necessarily be intimately related to the source of the solar wind. For studies of solar physics, changes in the gross structure of the corona reflect the 11-year cycle of surface activity; thus some of the more detailed coronal structures may be directly related to particular surface features.

The radiation that appears to come from the corona during an eclipse is composed of several components which are thoroughly described by Van de Hulst (ref. 1). The component due to atomic emission comprises no more than a few percent of the total radiation and arises only from the inner corona. The F, or dust, component is due to radiation from the solar photosphere that has been scattered to Earth by particles of interplanetary "dust" located anywhere along the observer's line of sight. The F component comprises most of the radiation apparently coming from the outer corona and is essentially unpolarized for the regime of small-angle scattering of interest here. The S_k or sky, component is photospheric radiation multiply scattered to the observer from outside the umbral shadow of the eclipse by particles in the Earth's atmosphere. The K, or electron, component is due to photospheric radiation that has been Thomson scattered by the electrons of the corona and thus is often referred to as the "true" corona. It is the largest component of the apparent radiation from the inner and mid corona (within 2.5 solar radii from the center of the solar disk) and is partially polarized by the scattering process.

Because of these properties of the K component, the three-dimensional structure of the coronal electron density distribution can be evaluated from white light photographs if

(a) The image size is sufficiently large

(b) The degree of polarization of the coronal radiation is measured by photographs taken through different orientations of a plane polarizer

(c) The photographs are calibrated in absolute radiance units

A complete set of such polarimetric observations has been obtained from the ground at a previous eclipse (Saito, 1962). A conspicuous coronal condensation observed there was reduced to a three-dimensional structure, and by application of hydromagnetic theory was fitted with magnetic tubes of force by Billings and Saito in 1964 (ref. 2).

In this study two additional tools were used to evaluate the structure of the electron density distribution: First, the observations were made from a high altitude aircraft so that the atmospheric scattering was reduced, thereby permitting structures of the K corona to be traced about six solar radii into the outer corona. Second, a special radial transmission filter was used to reduce the strong coronal brightness gradient, permitting a larger effective range of brightnesses to be recorded on a single photograph. On this eclipse, a flash spectrum of the chromosphere and inner corona was taken at second contact to provide supplementary information. (First contact is the instant when opposite solar and lunar limbs first appear to touch; second

contact occurs when the solar and lunar east limbs appear to coincide and the solar disk becomes completely obscured by the Moon.)

This paper describes the instrumentation and calibration procedures utilized and presents some of the initial results. Further analysis of structural features and polarizations to quantify the electron density distribution in detail remains to be deduced from our data.

The authors are deeply indebted to many persons for their support of these observations. In particular, we are indebted to Dr. Gordon Newkirk, Jr., for encouraging the continued development of the radial transmission filter and for supplying the calibrated brightness standards, and to William G. Ogles for doing the highly uniform processing of the two eclipse films. We would like to thank the managers of the eclipse expedition, Dr. Michael Bader and Lewis E. Haughney, and the CV-990 flight crew for providing one of the longest views of the corona in history. We appreciated the cooperation and suggestions of the following commercial representatives: John Darsow, William F. Swann, Edward Barr, and David Richardson. We thank Dr. Sidney Edelson for several fruitful discussions concerning eclipse astronomy.

INSTRUMENTATION

Figure 1 shows the complete system installed aboard the NASA CV-900 aircraft. The system is basically an apochromatic camera designed for airborne radiometric eclipse observations. With the exception of the radial transmission filter, the stabilization circuitry, and the camera control unit, all the basic components were obtained from either commercial or government surplus sources. The three items mentioned were designed, and all components were assembled, at Ames Research Center. The three-gimbal stable platform mounted on the main A-frame is the basis of the inertial stabilization of the line of sight. The lens and filter wheel support are located just above the white cone in the center of the photograph. Various power supplies, amplifiers, and recorders are visible. The closed observation window appears at the top center.

Optics

The optical train of the system is quite simple, as shown schematically in figure 2. The window is of high quality borosilicate crown glass, 13 inches in diameter and 1-1/4 inches thick. Its surfaces were polished flat to better than 6 fringes at $\lambda 6000$ over any 6-inch-diameter area and were coated to provide less than 1-percent reflection. The window was mounted normal to the line of sight at an elevation of 65°. Slightly warmed air blown across the cold inner window surface prevented the condensation of cabin moisture.

Because of the need for quick interchangeability, the various filters used were mounted before the lens. The wratten gelatin filters used had little noticeable effect on optical resolution, but the Polascreen (HN 42

Polaroid in grade B glass) generally degraded the system resolution to about 30 arcsec. The lens, a scaled-down version of the B.O. Morgan refractor of the Lowell Observatory, is an air-spaced Cooke triplet at f/16 with a 3-inch aperture. (Since the aperture stop and exit pupil coincide at the secondary principal plane about 1/4 inch before the first lens surface, the lens is free of distortion even with the various filters in place.) All six lens surfaces are coated to about 0.5-percent reflection to give a 90-percent net transmission for the visible region.

Immediately before second contact, a "straight-through" objective grating was inserted before the apochromatic lens, converting the camera into a slitless spectrograph. The 300 line/mm grating has a theoretical spectral resolution of 1/3 Å in the first-order red and is "straight-through" for λ5650. When coupled with the 48-inch focal length Cooke triplet, the grating provides a dispersion on the focal plane of 25 Å/mm at λ6400 and 23 Å/mm at λ4600.

To calibrate the camera plate scale, distance was measured on the original negatives to less than ±0.2 percent reading uncertainty with an optical comparator. Two separate lunar photographs taken at different times and locations gave the same plate scale (5.954 μ/arcsec) to within ±0.05 percent difference after corrections had been made for film shrinkage and lunar parallax. Photographs of the lunar terminator on Plus X film showed a total resolution that varied from about 3 to 5 arcsec over the 0.5° full field.

Based on this calibration, the optical effects of the aircraft window and boundary-layer turbulence were investigated to assess the limitations incurred by viewing from the CV-900. First, the resolution obtained on lunar photographs taken from the ground and from the aircraft was not discernibly different. Thus, boundary-layer turbulence was not observable at our 3-5 arcsec resolution level. Second, no asymmetric distortion was apparent (at the same resolution level) from measurements of polar and equatorial lunar diameters on the eclipse negatives. Third, the measured angular separation on the eclipse negatives of the star K Taurus from Jupiter, after correction for a 0.67 percent apparent minification due to a flat optical window of our thickness and refractive index, agrees to within 0.06 percent of the separation calculated from the ephemeris (ref. 3). Thus, for these two objects up to 1.75° off axis and 5773.4 arcsec apart, there was no measurable distortion due to window deformation.

Stabilization

To permit long exposures, the usual motion of the aircraft must be reduced and the camera should be isolated from the aircraft. Aircraft motion was reduced by careful control of the aircraft autopilot. Table I gives some representative figures for the frequency and average angular amplitude of the resultant aircraft motions as measured by Whittaker (ref. 4) during the long, nonturbulent portions of this eclipse flight. The most noticeable residual motion to the on-board observers was a 0.2-cps Dutch roll.

The camera was mounted on the innermost gimbal of a three-gimbal, gyroscopically controlled stable platform to isolate it from the residual motion. Figure 2 shows only a highly simplified schematic drawing of this platform and does not reveal the difficulty encountered in alining the three-gimbal axes with the aircraft axes without closing off the gimbal aperture for the camera. This situation was alleviated when the gimbal pitch and yaw axes were oriented about 30° away from their respective aircraft axes. The axes of the HIG-5 gyros were alined with the gimbal axes, not the aircraft axes. Since the gyro input signal is proportional to the cosine of the angle between the aircraft and gyro axes, the compromise did not seriously affect gyro sensitivity.

The most important factors in a gimbal mounting are balance and bearing friction. Clearly, if the camera were perfectly balanced on completely frictionless bearings, it would remain steady in space regardless of aircraft motion. Since such a self-stabilizing condition can only be approximated, each of the three axes of motion of the camera was separately stabilized in space by means of individual rate-integrating gyros mounted on the camera. The inherent gyro drift rates (anywhere from 1 to 60 arcsec/sec depending on the age and quality of the gyros) are nulled out of the system by visually tracking the celestial object just prior to making observations. With the input axis of each gyro mounted parallel to its corresponding gimbal axis, closed-loop inertial stabilization is obtained by completing the servo loop from the gyro to its corresponding gimbal torque motor as shown in figure 3. The main function of an assistant observer is to point the camera in the desired direction initially before uncaging the gyros. Generally, the system need be repointed only after very large disturbances.

Three main instrumental factors prevented the system from attaining optimum pointing stability. The stable platform used was primarily designed for the Thor rocket program; hence, its bearings were originally heavily preloaded for rocket launch stresses. Although much of the preloading was removed, there was not sufficient time before the eclipse to reduce the bearing friction caused by the original preloading. Consequently, the system's response was reduced. Also, because of this friction in such large bearings, the apparent static balance of our system was very poor and, in effect, placed a larger load on the gimbal torque motors. Finally, the frequency and amplitude of aircraft motions were learned only after the eclipse; hence, the system could not have been optimized beforehand for the dominant Dutch-roll motion of the aircraft.

The level of stabilization attained was determined from the measured motion of the Jovian image on the eclipse photographs and from records of the gyro error signals. The system was <u>not</u> capable of following the few large-amplitude, high-frequency motions caused by localized regions of turbulent air. The maximum peak-to-peak displacements of the line of sight from non-turbulent aircraft motion during the 9-3/4 minute duration of eclipse totality were less than 3 arcmin in roll and 1.5 arcmin in yaw or pitch. Average peak-to-peak displacements were about 1.5 arcmin in roll and 0.5 arcmin in yaw. The predominant error signal frequency observed was that of a 0.22-cps Dutch roll with roll and yaw error signals in phase. For photographic exposures of 2 seconds or less, the 80-pound camera often produced images showing less than

40 arcsec of motion. During one 0.05-second exposure, the error signal record indicated only 1/8 arcsec of motion in roll.

Camera Mechanization

The jarring impacts of the large K-24 camera shutter were completely isolated from the stabilized camera since the shutter was mounted onto the outer unstabilized support frame rather than on the camera itself. Thus, the shutter moved around inside the camera, about 2 inches in front of the focal plane. The mechanical supports of the shutter enter the camera through two side apertures which are covered by a few layers of loose black cloth.

Because of the different film-speed requirements for different types of coronal observations, two types of 70-mm film were spliced together in one roll. The frame of the 70-mm magazine was enlarged to 2 inches high by 4 inches wide to allow a 10 by 20 $R_{\odot}$ full field of view. A small microswitch was installed just beyond the lower right edge of the frame. A hole punched in the film near a splice actuated the microswitch which triggered a buzzer to indicate the presence of the splice and the change from one film type to another.

A step-wedge sensitometer calibrated each exposure by projecting a small pie-shaped image of a photographic step wedge through the open shutter onto the upper right-hand corner of the camera frame. The battery-powered tungsten source of this sensitometer was voltage controlled. A remotely controlled solid-state intervalometer automatically programmed film advance and exposure time through a sequence of 9 different exposures. These exposure times could be controlled in steps of factors of about 2 from 1/40 up to 10 seconds. Thus, with 4 seconds allowed between exposures for shutter rewind and film advance, a 9-exposure sequence is completed in 55 seconds. Exposures longer than 10 seconds were set manually into the intervalometer by means of shutter-open, shutter-close pulses. The program of 40 exposures (on two different films) shown in table II was successfully completed during the eclipse.

Another special mechanical feature of this camera is the means by which the Radial Transmission Filter (RTF) is positioned just before the focal plane for only one of the exposure sequences described above. The filter itself is just a small piece of black paper (its shape is described under Filter Design) used to partially occult the brighter inner corona. It is mounted at the intersection of three fine (0.005-in. diam.) wires stretched from a large ring whose diameter is just larger than the camera frame. The ring is free to rotate in a bearing race which can be moved into and out of the camera frame along two rails at the sides of the frame. A small motor drives the bearing race containing the RTF down (from its storage position above the camera frame) and positions the center of the RTF within 0.003 inch of the optic axis of the camera and less than 1/3 inch before the focal plane. Simultaneously, a jet of compressed gas blows on small turbine-like blades along the circumference of the mounting ring causing the ring to rotate faster than 600 rpm. The several impulses caused by starting and positioning the RTF disturb the camera stabilization momentarily, but after the ring is spinning in position

the disturbances are negligible compared to the aircraft motion. Starting and positioning of the RTF require about 30 seconds and are usually done while the film is changed from one type to another.

FLASH SPECTRUM

Because the time and the objective grating described earlier were available, a flash spectrum of the chromosphere was taken just about 2 seconds after second contact. The 1-second exposure was nearly optimum for recording the spectrum from λ4350 to λ6700 with this system. The lines are in best focus from λ5000 to about λ6300, primarily because the film plane of the system is not curved. At these wavelengths a chromatic resolution of 1 to 1.5 Å was realized. This corresponds well with the 12 arcsec of camera motion in aircraft yaw recorded during this exposure.

The usual features of the flash spectrum are present in the negative print of figure 4. Eight prominences appear on the east limb, one with a particularly strong continuous spectrum. Overlying the broad band of coronal continuum, the coronal iron lines at λ5303 and λ6374 appear as nearly continuous circles brighter in the northern hemisphere. The short arcs of the lower chromospheric lines contrast with the long broad arcs of the higher hydrogen and helium lines. Also, the continuous spectrum of Jupiter is present on the negative providing an intensity calibration. Some 50 lines, mainly chromospheric, are listed in table III with the major identifications made to date. All lines of HeI are present in the recorded region, but the presence of any HeII lines is questionable.

BRIGHTNESS OF THE TOTAL (K+F) CORONA

Photometric Analysis

The purpose of this analysis is to provide an absolute measure of the coronal brightness. This is done by comparing the coronal brightness to that of the solar disk (an absolute energy source) with an intermediate radiance standard prepared by Dr. Gordon Newkirk of the High Altitude Observatory. A standard inserted between the Sun and camera replaces the Sun by another known radiator whose brightness is on the order of that of the corona (10^{-6} to 10^{-9} $B_{\odot}$). Radiation from the standard traverses the optical train and excites the detector (film). Fine gradation of the film response is obtained from a photographic step-wedge attenuator mounted just before the film. The calibration is effected by comparing the film density caused by coronal radiation with that due to the solar disk, opal standard, attenuator wedge combination to obtain the coronal brightness in units of the average surface brightness of the solar disk ($B_{\odot}$).

The pair of intermediate standards was supplied by Dr. Newkirk to provide a uniform photometric basis for the intercomparison of our eclipse and his

balloon-borne coronagraph pictures. Each standard consists of a piece of uniformly exposed and developed photographic film sandwiched between two pieces of glass (one clear glass and one flashed opal glass). The Lambertian nature of the scattering by the opal glass and the manner in which it is illuminated by the Sun reduces the direct solar brightness to approximately 10^{-5} times its average value. The darkened film further reduces the brightness of the standards in full sunlight to 1.0×10^{-6} and 5.0×10^{-8} $B_{\odot}$, respectively, at $\lambda5540$. The standards were calibrated at three other wavelengths to about 10 percent at the High Altitude Observatory.

The eclipse photographs were actually calibrated two days after the eclipse. The calibration consisted in making sequences of exposures that duplicated the eclipse exposures in all respects except that they were made on the uneclipsed Sun with an opal standard in front of the camera optics and a large calibrated attenuator wedge mounted directly before part of the camera frame. To insure that the shutter response was truly repeated between calibration and eclipse exposures, the small pie-shaped sensitometer wedge described earlier was projected through the shutter onto one corner of the frame. (The small sensitometer wedge is in addition to the large attenuator wedge.) The eclipse films were hand developed in a stainless steel tank along with their calibrations after being presoaked in water for 4 minutes at 68° F. The Plus X Pan exposures of the total (K+F) corona were overdeveloped in D-76 to a γ of 1.4. All other exposures, including those on 2475 Recording Film, were developed to a γ of 0.7 in D-76 to increase the scale and reduce grain. The uniform illumination of the camera frame by the flashed opal and the improved uniformity of development due to presoaking are both apparent in figure 5, a microdensitometer trace of one of the more contrasty calibrations. In general, all development fluctuations remained below 0.05 D unit.

To maintain a consistent calibration, all negatives were read on the same commercial instrument, a two-dimensional scanning microdensitometer (Isodensitracer). After the two-dimensional scan of the photographs, the instrument was converted back to a one-dimensional microdensitometer to read the calibrations. For the following three reasons it is felt that all readings, which are densities above base fog, are accurate and internally consistent to better than ±0.02 D unit. First, the instrument is basically a null-reading device; second, no apertures or filters were changed during the readings; third, the instrument was re-zeroed within ±0.015 D unit of the film's base fog whenever a lamp bulb was replaced.

To determine the relative brightness of the corona, these data were directly evaluated by means of the "characteristic curve," a plot of density observed versus the common log of the radiant energy per unit area incident on the film (fig. 6). If the gradation of the step-wedge attenuator is fine enough, this process becomes essentially one of finding a null balance between the density produced by the observations and that produced by the calibration. When the density difference is expressed as a linear logarithmic function and integration is performed over the wavelength interval responsible for the observed densities, the equation describing the observation-calibration balance is

$$\frac{D_{cor}(r) - D_{op}(\text{step no.})}{\gamma} = \log_{10}\left[\frac{f_{cor}(r)\int_{\lambda_-}^{\lambda_+} B_\odot(\lambda)S(\lambda)T_{WFL}(\lambda)d\lambda}{T_W(\text{step no.})\int_{\lambda_-}^{\lambda_+} N_W(\lambda)f_{op}(\lambda)B_\odot(\lambda)S(\lambda)T_{WFL}(\lambda)d\lambda}\right]$$

where

$B_\odot(\lambda)$ average surface brightness of the solar disk

$D_{cor}(r)$ density of the coronal photograph at position (r) off axis

$D_{op}(\text{step no.})$ density of the calibration photograph behind a particular step of the attenuating wedge

$f_{cor}(r)$ relative brightness of the corona at (r) in units of the average surface brightness of the solar disk

$f_{op}(\lambda)$ relative brightness of the flashed opal standard in units of the average surface brightness of the solar disk

$N_W(\lambda)$ spectral specular transmission of the wedge normalized by its own average value over the wavelength interval (λ_-,λ_+)

$S(\lambda)$ spectral response of the film

$T_W(\text{step no.})$ integral diffuse transmission of a particular step of the wedge

$T_{WFL}(\lambda)$ product of the spectral transmissions of the aircraft window, any filters, and the camera lens

γ $\dfrac{\Delta D}{\Delta \log_{10}\left(\frac{\text{energy}}{\text{area}}\right)}$, slope of the characteristic curve

λ_-,λ_+ limiting wavelengths for the system

In this equation, the exposure times and relative apertures have already been canceled because they were constant from observation to calibration. It is well known that the relative brightness of the corona $[f_{cor}(r)]$ is essentially independent of wavelength because the coronal radiation is predominantly Thomson scattered radiation from the solar surface. For short wavelength intervals and for attenuator steps with densities less than 2, the spectral transmission $[N_W(\lambda)]$ of the attenuator wedge varies by less than 10 percent. Thus, if the relative brightness of the opal standard $[f_{op}(\lambda)]$ were also flat over the wavelength region in use, the integrations over the product BST would cancel leaving the direct result that when the left side of the equation is zero

$$f_{cor}(r) = T_W(\text{step no.})f_{op}$$

Balancing the densities directly through the characteristic curve is useful because it permits interpolation across small density intervals between attenuator steps, and because regions of the curve where the slope γ only slowly varies may also be utilized.

With present computer techniques it is not difficult to do the actual integrations shown, so that reliance on the spectral flatness of the various media is unnecessary. In addition to improving the accuracy of the method, this also permits enlargement of the wavelength interval used so that the "speed" of the system is effectively increased, a useful gain for airborne eclipse measurements. The flashed opal brightness at wavelengths other than those of the four HAO calibration wavelengths was determined from the normalized specular transmission of the opal standards as measured on a scanning spectrophotometer. The only other function of wavelength not known or easily measured is the spectral response of the film, $[S(\lambda)]$. Since the wavelength dependence of the spectral response is essentially independent of any specified density level, processing condition, or exposure time (ref. 5), the curves of "sensitivity" supplied by the film manufacturer as "representative of the current product" may be used directly to evaluate the integrals. The result of the integrations in the case of Plus X Pan film and flashed opal number 1 is that the integrated value of the relative opal brightness is 4 percent greater than its simple average value on the same wavelength interval. A simple error analysis based on a random distribution of all measurement errors indicates that the integrated calibration should provide an absolute measure of the coronal brightness to within ±16 percent in the absence of systematic error.

Scattering Within the Optical System

Even before the absolute calibration described above was completed, an unmeasured systematic error was apparent in the photometric analysis. The ellipticity of the isodensity traces produced by the two-dimensional microdensitometry was measured and compared with the ellipticity of the coronal isointensity curves (isophotes) reported for this eclipse by Prof. Waldmeier (ref. 6). Although our ellipticities have the same general dependence on off-axis distance as Prof. Waldmeier's, they were generally 25 to 30 percent less than his. Also, our ellipticities were somewhat lower than observed at other eclipses near solar minimum (ref. 7). The apparent decrease in ellipticity could easily be caused by uniformly scattered light within the optical system; the following scattering experiment was performed to investigate the order of magnitude of this possible source of systematic error.

The scattering experiment is designed to measure the fraction of incident coronal brightness that is scattered a specified distance off axis by the optical system itself. In the laboratory it consisted in shining a model of the bright inner corona on the camera and photographing the faint light scattered outside the model image. The light scattered beyond 1.5 $R_\odot$ (outside

the model image) is first recorded on photographs of the undimmed model made with a paper occulter completely covering the model image in the focal plane of the camera. Next, the occulter is removed, the model is dimmed by neutral density filters, and exposures of duplicate duration are made of the model itself. By means of a new characteristic curve, the scattered density and model density are nulled to zero as before, producing in this case the fraction of incident flux scattered in terms of the transmission of the neutral density filters. Because a particular step of the model must be selected to effect the comparison of densities, the fraction of off-axis scattering must be expressed in terms of that particular step. However, the ratio obtained still represents the fraction of the total coronal brightness scattered because each step is directly related to its proper position in the coronal brightness gradient through the model construction.

The construction of the azimuthally uniform model of the radial brightness distribution of the inner corona followed a method described by Dr. S.E. Stone of Los Alamos Scientific Laboratory (personal communication, 1965). Gelatin neutral density filters with apertures of gradually increasing diameter were superposed concentrically in a 3-1/4 by 4-inch projector slide frame. The densities of these filters were selected to duplicate the azimuthally averaged coronal brightness gradient of this eclipse to within 10 percent by again referring to the data of Prof. Waldmeier. The model was back projected onto a translucent diffusing screen and front-viewed by the camera system in a completely darkened room. Care was taken to prevent excessive heating of the gelatin filters of the model during the observations. The direct image of the model in the focal plane of the camera was covered with a paper occulter so that for this set of exposures only light scattered in the optical system could reach the film. A second set of duplicate exposures was made immediately thereafter but with the occulter removed and with the overall intensity of the model reduced three to four orders of magnitude by a sandwich of gelatin neutral density filters inserted between the projector and the screen. The transmission of the gelatin filter sandwich was measured shortly after the observations on a diffuse densitometer. Both sets of exposures were simultaneously developed in a stainless steel tank and then measured on a microdensitometer. Characteristic curves for each frame were constructed from the densities produced by the small sensitometer wedge impressed through the shutter on each exposure. The differences in density produced by the scattered light and the light from the dimmed model were read directly against the individual characteristic curves to give the logarithm of the ratio of scattered intensity to the intensity incident in the step of the model at 1.25 $R_{\odot}$. Although this method of photometric analysis is not as accurate as that used in the preceding section, the data were internally consistent to better than 15 percent.

The scattered intensity was distributed with azimuthal uniformity and was unpolarized as would be expected. The fraction of the incident intensity scattered was determined as a function of off-axis distance from six pairs of exposures. These exposures differed only in that the scattering elements of the optical system differed. Thus, the major scattering element in the system can be determined by a comparison of the fractions scattered. In figure 7, the fraction of the incident intensity that was scattered is plotted as

$N_s(r)/N_{IM}(1.25)$ for lens alone, lens plus window, and lens plus window plus filter. (The off-axis distance r is scaled in units of one solar radius on the film plane.) It is clear from these curves that the predominant scattering element in the optical train was the aircraft window, which produced about six times as much scattering as the lens alone. It is not surprising that the window is the major contributor to scattering. First, the passage of the aircraft through dense rain clouds shortly after takeoff from Hilo washed a considerable amount of dust and dirt onto the window from the top of the aircraft. Secondly, the lens was mounted 2-2/3 feet from the outer window surface rather than close to it, so more window area could contribute to the scattering.

The most significant parameter in the scattering problem is the ratio of scattered brightness to coronal brightness at the same off-axis distance. This systematic error could possibly degrade the absolute calibration of the photographs significantly. To evaluate this parameter, the scattered brightness at distance r was determined by multiplying the fraction of the model intensity scattered from the lens plus window plus filter curve by an azimuthal average of the solar minimum K+F coronal brightness at 1.25 $R_\odot$ given by Allen (ref. 8). These values of the scattered brightness were then divided by Allen's values of the F component brightness at the same distance r to give what shall be called the F component scattering ratio,

$$S_F(r) = \left[\frac{B_s(r)}{B_c(r)}\right]_{F \text{ component}}$$

When the same brightnesses are divided by Allen's equatorial K+F values for solar minimum, the following (K+F) scattering ratio is obtained

$$S_{K+F}(r) = \left[\frac{B_s(r)}{B_c(r)}\right]_{\substack{K+F,\ \min \\ \text{equator}}}$$

These functions are plotted as the upper two curves in figure 7. Using Allen's data in both the numerator and denominator of these ratios cancels the errors due to different absolute calibrations. In view of the errors due to diffuse densitometry, different tungsten lamps, the coronal model, azimuthal averages, and the variable dust content of this system, these curves probably represent an upper limit of the actual ratio of the scattered to the coronal brightness only within 40 percent.

The flatness of the F component scattering ratio is at first quite startling. It is fortunate for the separation of the F component from the instrument scattering that the ratio is 10 percent or less, for if it were not, one could never be certain that the source of the F component was truly outside his system. The explanation of the flatness of this ratio within 6 $R_\odot$ is apparent when it is realized that both the instrument and the F component scatter are cases of small-angle scattering from large particles. The Mie effect (a complete solution to the problem of scattering by large spherical metal or dielectric particles, ref. 9) shows that the angular scattering functions are maximal for all types of small-angle forward scattering. Thus, the

variation of off-axis angle from 0.5° to 1.5° (2 to 6 $R_\odot$) corresponds only to small changes in the angular scattering functions of both the instrument and the F component because these functions have already closely approached their maximums.

Since at solar minimum the polar corona beyond 1.5 $R_\odot$ is largely due only to the F component, the F component scattering ratio closely represents the ratio of instrument scatter to the total (K+F) brightness in the poles. With this interpretation then, a comparison of the upper two curves of figure 7 clearly shows that instrumental scattering consistently adds a higher percentage of radiation to the polar regions than to the equatorial regions. This effect is definitely responsible for the observed reduction of isophote ellipticity which stimulated this study of scattering.

The most important characteristic of both these scattering ratios is that neither curve exceeds 10 percent. Because the aircraft passed through the rain cloud before the eclipse, these data almost certainly represent an upper limit for instrument scattering during a natural eclipse. The low level of scattering is important not only from the point of view of absolute calibration, but also with respect to the degree of coronal polarization observed. Since the scattered radiation is unpolarized, the degree of polarization of the corona observed through a plane polarizer is reduced from what it would have been in the absence of scattering by the factor $[1 + S_{K+F}(r)]^{-1}$. Since $S_{K+F}(r)$ varies somewhat with distance and azimuth, it is indeed fortunate that the level of scattering is so low. Few coronal theories are sensitive to observational errors in absolute brightness or degree of polarization of less than 10 percent.

Calibrated Isophotes of the K+F Corona

The primary objective of this entire section is to present figures 8 and 9 in such manner that the reader can correctly find the intensity of the K+F corona at any desired point. In addition to the photometric calibration and the correction for instrumental scattering previously described, an accurate center for the solar disk and a correction for sky background must be given.

Figures 8 and 9 are reproductions of the two-dimensional microdensitometer scans of the 0.2 and 5.0-second exposures on Plus X Pan film taken at $21^h28^m26^s$ and $21^h28^m45^s$ U.T., respectively. (Figures 5 and 6 are the calibration of figure 8.) In figures 8 and 9, an increasing intensity gradient is indicated by the progression of the writing mode from lines to dots to clear spaces to lines, etc. Within the innermost corona, the higher densities exceeded the range of the instrument so a uniform signal was recorded. Also, in the inner corona the rate of change of intensity exceeded the writing rate of the instrument so that before the instrument became saturated, the different writing modes often became unintelligible. The sensitometer wedge is shown in the upper right-hand corner of the figures. The large drying mark on the negative (outlined on the right side of fig. 9) is a small density discontinuity of less than 0.03 D unit so that correct isophotes can be visually traced across it. The planet Jupiter, conspicuous in the photographs of the next section, appears here as a small discontinuity on the right-hand side of

the figures. The star K Taurus appears in the upper right-hand corner of figure 9. Uniform camera motion is evident in figure 9 both from the increased Jovian diameter and from the uniformly reduced lunar diameter.

Because of the steep brightness gradient of the inner corona, a small error in locating the center of the solar disk can appear as a large photometric error. The solar center was located on these figures by means of the position of Jupiter, the lunar limbs, the time, and a line of solar centers calculated from routine ephemeris data. Corrections to right ascension and declination for lunar parallax were made. Centering was checked by the K Taurus-Jovian-solar triangle where possible. The resulting centering error on these 5 times enlarged microdensitometer scans is about 3/4 mm or 24 arcsec. This could amount to no more than 12-percent intensity error in figure 8, and a 7-percent intensity error in figure 9. The position of the solar limb is indicated by a circle in each figure and a distance of one solar radius is accurately laid off beneath the figures. Position angle is indicated every 10^{o} counterclockwise around the edge of the frame.

The value of the background skybrightness (S component) was determined at 9 $R_{\odot}$ in the extreme NE and SW corners of figure 9. Note that there are no streamers at these particular position angles. The brightness near each corner is 5.3×10^{-10} $B_{\odot}$. If 1.3×10^{-10} $B_{\odot}$ is attributed to the K+F components (ref. 8), the value for sky background is 4×10^{-10} $B_{\odot}$. This same value for sky background was also observed in 1963 by Ney's group (ref. 10) from the DC8 at 40,000 feet, with only a 48^{o} elevation. If one follows their arguments for decreased sky brightness with increasing elevation angle, the higher solar elevation of this eclipse should have produced a lower sky brightness. It is quite possible that the change in albedo of the terrain beneath the airborne observers (from forest to ocean) compensated for the reduction due to higher elevation angle. However, the photometric accuracy of measurements at the very corner of a camera frame is also questionable because of development edge effects.

The instrumentally scattered brightness was obtained from the preceding section by multiplying the ratio $[N_S(r)/N_{IM}(1.25)]$ from the lens plus window plus filter curve by Allen's K+F brightness at 1.25 $R_{\odot}$ (ref. 8). The constant sky background was then added to produce the total correction for instrumental and sky scattering given in table IV. Finally, the photometric calibration of each microdensitometer scan from the characteristic curves presented under Photometric Analysis is given separately on each figure.

To obtain the K+F brightness in either figure, count the number of lines from the base fog of the negative up to the point of interest. The photometric calibration on the figure gives the raw brightness of the region. The value of instrumental and sky brightness for the off-axis distance of the region (table IV) is subtracted from the raw brightness to yield the correct brightness. As one counts the number of lines above fog on the figures, each change of writing mode is approximately one-third of an intensity step so that interpolation to one-sixth of a step between lines is often valid.

In addition to figures 8 and 9, two-dimensional microdensitometer records of the 0.05 and 1-second exposures on Plus X Pan film were studied to determine the absolute calibration and internal consistency of the data. The polar regions of the corona were used for these comparisons because the F component is the chief source of coronal brightness beyond 1.5 solar radii. Because the F component is essentially constant in both time and position angle, it provides a region in which both the absolute and relative calibration of the data can be examined independently of effects due to varying coronal structure. As noted in the following section, even on the RTF photographs, the fine structure of the polar rays has faded by 2.5 $R_{\odot}$. At the much lower resolution of the microdensitometer scans, this fine polar structure is not evident at 1.3 $R_{\odot}$.

The four microdensitometer records were read north and south along the polar axis from 1.2 $R_{\odot}$ to 4.4 $R_{\odot}$ and at position angles 10° on either side of the axis. Of these four records, usually two and often three could be compared for consistency of the brightness values at specified coronal positions. The greatest difference noted between any two records at the same point was always less than 35 percent. The largest differences occurred within 2 $R_{\odot}$ and decreased with increasing off-axis distance. Most differences were less than 16 percent. A north-south centering error would be evident on the decreasing gradient of polar brightness as an initially large, consistently north-south intensity difference on any single densitometer record. This difference would decrease, but would not vanish with increasing off-axis distance. The consistent north-south intensity differences actually observed on the individual records were all less than 16 percent. Such differences are in accord with about three-fourths the maximum possible centering error of 12 percent mentioned earlier and indicate that centering errors have less effect than the random photometric errors. The total random error for any one microdensitometer record is then estimated by taking the square root of the sum of the squared centering and photometric errors. From the differences just described, the total random error appears to be definitely less than ±18 percent anywhere and generally less than ±13 percent beyond 2 $R_{\odot}$.

So that the absolute calibration error could be examined, the data of the four records described above were further averaged over the three different position angles measured to form north and south average polar brightnesses. The variation of these polar brightnesses with distance is shown in figure 10 by the pairs of unenclosed dots. These may be compared to the curve taken from Allen (ref. 8) for the polar K+F corona at sunspot minimum. The agreement of these polar averages with Allen's data from many previous eclipse observations is excellent, particularly beyond 1.8 $R_{\odot}$ where the steady F component predominates. The small scatter of the average brightness values about the curve masks what absolute calibration error is present. However, the data are highly consistent with the ±10 percent "repeatability" error of the calibration of the flashed opal standards. Thus, it is clear that the absolute brightness of the corona can be obtained from figures 8 and 9 to within ±18-percent maximum error and most likely within ±13 percent beyond 2 $R_{\odot}$.

Another reason for thoroughly examining the accuracy of these observations is that the pilot study of our brightnesses indicated a moderate difference from the absolute brightnesses presented by Prof. Waldmeier in December 1965 (ref. 6). It was initially assumed that a detailed study of our data would result in a large reduction of that discrepancy. However, this was not the case. At present, Waldmeier's brightnesses are smaller than ours by a consistent factor of 1.8 in the polar regions from 1.7 to 4.4 $R_\odot$. Attempts are being made to resolve this difference.

A slight tendency for the northern brightness beyond 1.8 $R_\odot$ to exceed the southern brightness by about 5 to 10 percent is apparent in our data. Although it is reasonable for the K (electron) component to reflect hemispheric differences in solar activity, this explanation does not apply to the F component radiation which is scattered off interplanetary dust. Thus, beyond 1.8 $R_\odot$ any north-south polar brightness difference is probably not real.

The structural variations of the brightness of the corona are more apparent in the RTF photographs of the following section than they are in the densitometric presentations of figures 8 and 9. There are three reasons for this. The photographs were specially printed to retain as much structure in the prints as possible, while figures 8 and 9 are direct logarithmic representations. Secondly, figures 8 and 9 have a fairly low final resolution because of their long scale intensity range. Third, and most important, the structural variations are characteristic of only the K corona, whose average brightness is normally less than the F corona by 1.5 $R_\odot$ in the polar regions and by 2.5 $R_\odot$ in the equatorial regions. However, careful study of the figures does show the photometric shape of the main streamers at the position angles 082°, 103°, 330°, and 300°. The dim region directly above the coronal condensation at 290° (referred to in the following section) and the bright region just below it at 270° are also evident. Again, the relative faintness of the region at 290° is not so pronounced in these figures as in the RTF photographs for the reasons just mentioned. To illustrate both the azimuthal uniformity of the F component and the large extent of the "polar region" apparent on photographs taken near sunspot minimum, the brightnesses at position angle 235° are plotted in figure 10 (circled points) for comparison with the north and south polar axis brightnesses. Beyond 1.8 $R_\odot$ all measured differences are less than 15 percent, indicating that the polar corona covers a very large region near sunspot minimum, in this case, over position angles ±55° from the south polar axis. Except for the polar rays it is quite uniform. In contrast with the polar data are the brightnesses plotted as squares in figure 10. These were obtained at a position angle of 300° which runs fairly near one of the largest streamers. Within 1.8 $R_\odot$, where the effects of the F component can be neglected, this streamer is consistently brighter than the polar regions by a factor of 3. The factor falls off with distance as the F component dilutes the K coronal brightness.

It has been shown that the absolute brightness of the K+F corona can be determined from figures 8 and 9 to definitely better than ±18 percent and generally to within ±13 percent beyond 2 $R_\odot$. Dimensionally stable 8 by 10 inch prints of the complete set of four microdensitometer records (including

figs. 8 and 9) from which the brightnesses of figure 10 were obtained are available on request from the Technical Information Division, Ames Research Center.

CORONAL PHOTOGRAPHS WITH A RADIAL TRANSMISSION FILTER

Filter Design

As for the 1963 eclipse (ref. 11), a Radial Transmission Filter (RTF) was prepared that reduced the apparent coronal brightness gradient so that inner and midcoronal densities stayed well within the scale of Plus X Pan film. Because the grain of the film base used in the 1963 Radial Density Filter impaired resolution, the new filter was not made on film but rather was a rotating disk like that used to make the exposures for the 1963 filter. The shape of the new filter was determined in the same way, namely, from some desirable brightness curve drawn beneath the Van de Hulst (ref. 1) model of total coronal brightness so that it specified the effective filter transmission (T) as follows:

$$T(r) = \frac{[B(r)]_{\text{desired}}}{[B(r)]_{\text{VdH model}}} = \frac{\theta(r)}{\pi}$$

Here θ is the azimuthal coordinate of a polar coordinate curve, B a specified brightness, and r a radial distance in the film plane given for this eclipse by $r = (\text{focal length})(R_{cor}/R_{\odot})$ $(4.58\times10^{-3}$ rad). The parameter r is also the plane of the sky coronal distance from the center of the disk in units of one solar radius. There are two guide lines for drawing a "desirable" brightness curve. First, the curve should not be perfectly flat because the entire coronal gradient would be transferred to the RTF which then would have to be kept centered on the coronal image with extremely high accuracy. On the other hand, the curve should not have the same slope as the coronal gradient (i.e., a constant transmission filter) for then no gradient reduction is achieved. A compromise curve between these two extremes is desired. The coordinate $\theta(r)$ was plotted on stiff polar coordinate paper and the form cut out. The resultant shape, shown in figure 11, was suspended by wires from a ring which was rotated faster than 600 rpm just before the film plane as described under Camera Mechanization.

The preceding photometric analysis has not been applied quantitatively to the RTF photographs for two reasons. Although T(r) is precisely known for the RTF itself, it is not effectively known for any particular combination of exposure time, rotation speed, film type, and radius because of the photographic reciprocity and intermittancy effects (ref. 5). Although intermittancy becomes less complicated at high rates, it would still be very difficult to evaluate here because both the aperture and the source radiance are rapidly varying functions of radius. The other reason is that despite the stabilization of the line of sight, pointing was not necessarily centered on the lunar disk to better than 2 arcmin. Thus, the desired brightness

gradient was only approximately achieved, which is all that is required for structural photography of the corona.

Structural Features of the May 30th Corona

Figures 12 through 15 are fourth generation prints of 0.5, 1, 5, and 10 second exposures made through the RTF about 3 minutes before third contact. A special contact printer (Fluor-O-Dodge) was used to dodge the RTF negatives automatically as they were printed onto high contrast, fine grain film. Distortion-free negative enlargements were then made from which the fourth generation positive prints of the figures were made by conventional contact printing methods. The shorter exposures are particularly clear because camera motion was less than 20 arcsec. The result of the dodging by the RTF and the Fluor-O-Dodge is apparent in these prints where detailed coronal structures can be followed over radial extents of 3/4 to 1 $R_\odot$ on any one print. (Across such distances, the actual coronal brightness can vary by factors from 30 to 100.) The supporting wires of the RTF caused two photographic artifacts where the wires join the edge of the occulting disk. The single wire intersecting the disk edge at 4 $R_\odot$ creates (by scattering) a slightly brighter ring of about 0.4 $R_\odot$ width, which is evident on the 10-second exposure. The two wires that symmetrically intersect the edge of the occulting disk at 1.9 $R_\odot$ reduce the filter transmission at that radius by an amount proportional to their thickness. The resultant dim ring is noticeable on the 5- and 10-second exposures. These are the only two artifacts introduced by the RTF and they demonstrate the azimuthal uniformity of the filter's transmission.

Considering all four exposures, one can clearly discern the following features: five prominences (P), two sets of coronal arches, one permanent condensation (c), three large streamers out to about 6 $R_\odot$, polar rays out to about 2.5 $R_\odot$, and one long thin featherlike structure in the northwest. The planet Jupiter is conspicuous in the southwest and its image gives an accurate measure of camera motion. In addition, the stars K Taurus and H. D. 27946 are just discernible in the northwest corner of the frame.

One significant fact stands out from these photographs of the corona near sunspot minimum. First, note that the dodging by the RTF has perfect azimuthal symmetry and that the effect of Fluor-O-Dodge printing is to reduce large spatial brightness variations. These photographs still show a strong brightness decrease over extended polar regions (confirmed by the photometry of the preceding section) in addition to discrete fine structure. It is then clear from the Thomson scattering origin of the K component that the coronal electron distribution, particularly near the transition from equatorial to polar regions, is neither uniform nor spherically symmetric near the minimum of the sunspot cycle.

In the following discussion of coronal structure, reference will occasionally be made to surface features or activity not directly observable on the eclipse photographs. The source of information about these features is a sequence of the daily Fraunhofer maps of the solar surface (ref. 12) for the three weeks before and after the eclipse.

The structure of the northern hemisphere of the corona is particularly interesting. In addition to the conspicuous polar rays, there is the long (~3.5 $R_\odot$) thin structure in the northwest that has a size and shape intermediate between the characteristic forms of the polar rays and equatorial streamers. It is located at the position angle (330° to 340°) where the general coronal form changes from equatorial to polar. Apparently, it is a transitional type of structure. Because of its isolation from the general coronal background, it will become the subject of a thorough electron density study.

Symmetrically on either side of the northern rotational axis (±35° position angle) are two regions with predominant arch-system structure. These regions are the northernmost structures of the general form of the equatorial corona and are about three times brighter than the average polar region. Both regions have underlying prominences and plages, and both regions appear to extend into the outer corona as moderately large streamers. P. A. Sturrock has recently provided a theoretical interpretation of one of these arch systems (private communication).

Other than several small prominences (filaments), there was very little equatorial surface activity within ±45° of the east limb. However, the equatorial regions of the eastern corona are occupied by two large streamers which extend out some 6 $R_\odot$ on the negatives. The only noticeable structure within the fan or base of the largest streamer is an arch system centered at position angle 080°. Although the center arch appears small, it should be noted that larger but fainter concentric arches appear on the negatives as far out as 1.4 $R_\odot$ and that the entire base of the streamer is filled by this faint system. Because of the faintness of these outer arches, the streamer base appears quite uniform at first glance. Although not visible late in the eclipse when the RTF photographs were made, the small prominence within 1° of position angle of the center arch is evident (through its line and continuum emission) on the flash spectrum made at second contact. These features of the eastern hemisphere are representative of a generally quiet corona near sunspot minimum.

The equatorial regions of the western corona are dominated by a permanent coronal condensation (position angles 290° to 300°) associated with an underlying sunspot group of moderate size and very recent formation (~22 days old). An authoritative classification of this permanent condensation has been done by G. W. Curtis, F. Q. Orrall, and R. B. Dunn from their excellent spectra of this eclipse (unpublished data). As is characteristic of a center of activity at this early stage of development (ref. 7), high flare activity had been observed from this region during the preceding 14 days of its passage across the solar disk. Most of these flares were of Importance I, as might be expected at this stage of the solar cycle. The plate scale of this camera is too small for definite identification of the usual "knots" of material at the center of the condensation, but a hint of the characteristic large-loop prominences, seen diagonally, is present on the negatives. The mid corona above the condensation appears to be composed of long rays and clumps of material generally oriented toward a focus at the condensation. The overall curvature and orientation of these structures is concave outward. Further out, the

longer exposures show that the outer corona appears to become quite striated above the condensation as these rays and clumps take on an apparent radial orientation away from the center of the disk rather than from the condensation. Because of this apparent loss of the geometric source, and because, even with our different dodging techniques, the inner corona is still somewhat overexposed, the presence of the condensation is thoroughly hidden on those exposures of long enough duration to show the outer corona. Note that a largely overexposed inner corona and a mid to outer corona consisting of generally radially oriented rays, clumps, or bundles are characteristic of most coronal photographs taken near the peak of solar activity at sunspot maximum.

As is evident on these photographs, the entire coronal structure above the young center of activity contrasts strikingly with the large streamer shapes of the eastern corona over a relatively undisturbed solar surface. A thumbnail description of the overall structure of the corona apparent at this eclipse would have to be that the poles and eastern corona were at solar minimum while the western equatorial corona was approaching solar maximum. The contrast of the structures in these two regions is striking evidence of the manner in which a center of activity on the solar surface disrupts the form of the undisturbed minimum corona.

That a large hole (figs. 12 and 13) appears to have been blown out of the mid corona above the condensation is sustained by two observations. First, some 55 to 65 Importance I flares were observed at the young center of activity over the preceding 14 days implying a high particle pressure from that surface region. Second, the isophotes (described in the preceding section), even in the presence of the F component background, show a definite depression in the mid corona (beyond 2 $R_{\odot}$) above the condensation indicating a generally lower average electron density. The overall geometry of the coronal structure above the condensation is quite consistent with the concept of <u>open</u> magnetic lines of force in contrast with the arches on the opposite (quiet) limb that are more consistent with <u>closed</u> lines of force. Possible particle trajectories or flux tube channels from the condensation through the corona are apparent as rays and clumps (as mentioned earlier). Additionally, it is quite simple to mentally construct a typical picture of the sunspot maximum corona by randomly superimposing on a minimum corona many structures similar to this one. It is clear that further study of all information pertaining to this young center of activity, including electron densities yet to be reduced from our data, is desirable to test the exciting conjectures of this paragraph.

Ames Research Center
National Aeronautics and Space Administration
Moffett Field, Calif., 94035, Dec. 16, 1966
188-38-01-08-00-21

REFERENCES

1. Van de Hulst, H. C.: The Solar System. Vol. I of The Sun, G. P. Kuiper and B. M. Middlehurst, eds., Univ. of Chicago Press, 1953, p. 256.

2. Billings, Donald E.; and Saito, Kuniji: Polarimetric Observations of a Coronal Condensation. Ap. J., vol. 140, no. 2, Aug. 1964, pp. 760-777.

3. Anon.: The American Ephemeris and Nautical Almanac. U. S. Government Printing Office, Washington, D. C., 1965, pp. 178, 286, 308, 314, and 332.

4. Cameron, R. M.: Douglas Tasks for Airborne Solar Eclipse Expedition of May 30, 1965. SM-48792, Douglas Aircraft Corp., 1965, p. 80.

5. Mees, C. E. K.: Theory of the Photographic Process. MacMillan Co., 1942, pp. 250 and 687.

6. Waldmeier, M.: The Brightness Gradient of the Corona at the Solar Eclipse of 30 May 1965. Z. Astrophys., vol. 63, 1966, pp. 242-266.

7. De Jager, Cornelius: Structure and Dynamics of the Solar Atmosphere. The Solar System. Vol. 52 of Handbuch der Physik, S. Flügge, ed., Springer-Verlag (Berlin), 1959, pp. 184 and 253.

8. Allen, C. W.: Astrophysical Quantities. Second ed., Athlone Press (London), 1963, p. 176.

9. Born, M.; and Wolf, E.: Principles of Optics. Second ed., MacMillan Co., 1964, p. 653.

10. Gillett, F. C.; Stein, W. A.; and Ney, E. P.: Observations of the Solar Corona From the Limb of the Sun to the Zodiacal Light, July 20, 1963. Ap. J., vol. 140, no. 1, July 1964, pp. 292-305.

11. Smith, S. M.; Bader, M.; Torrey, R. A.; and Henderson, M. E.: A Stabilized Automated Camera for Airborne Eclipse Photography. ISA Trans., vol. 3, no. 3, July-Sept.1964, pp. 212-219.

12. Anon.: Daily Map of the Sun, May 12 through June 18, 1965. (Freiburg im Breisig: Fraunhofer Institut).

TABLE I.- CV-990 MOTION DURING 1965 ECLIPSE (REF. 4)

Frequency, cps	Average angular amplitudes, degrees peak to peak		
	Roll	Pitch	Yaw
5	0.2	0.08	0.04
.2	.4	.1	.2
.01	1.4	.2	.8

TABLE II.- EXPOSURE PROGRAM

Subject	Optical accessories	Exposure times, sec	Film	Development contrast, γ
Flash spectrum	Objective grating	1 and 5	2475 recording film	0.7
K corona	Polaroid, 60° forward Polaroid, vertical Polaroid, 60° aft	0.1, 0.2, 0.5, 1, 2, 5 0.1, 0.2, 0.5, 1, 2, 5 0.1, 0.2, 0.5, 1, 2, 5	2475 recording film	.7
Coronal structure	Radial transmission filter and wratten 8	9-exposure sequence plus one 30-second exposure	Plus X Pan	.7
K+F corona	Wratten 2A	9-exposure sequence plus one 30-second exposure	Plus X Pan	1.4

TABLE III.- CHROMOSPHERIC FLASH SPECTRUM TWO SECONDS AFTER SECOND CONTACT, MAY 30, 1965

Line number	Identity	Relative density (preliminary)	λ, Å
1	(TiII, NdII, FeI)	Thinnest	4368-4369
2	FeI	Thinnest	4376
3	HeI	Very thin	4388
4	TiII	Very thin	4409
5	(CaI, HeI)	Thin	4435-4437
6	HeI	Dense	4471
7	[a](TiII, FeI, FeI)	Thin	4493-4494
8		Very thin	4513
9	[a](FeI, BaII)	Thin	4525
10	[a]FeII	Thin	4541
11	(BaII, CrII)	Medium dense	4554-4555
12	[a](FeI, FeII)	Thin	4556
13	[a]TiII	Thin	4563
14	[a](CrI, TiII)	Thinnest	4572
15	HeI	Medium dense	4713
16	[a](FeI, FeII)	Thinnest	4818
17	HI(H_β)	Densest	4861
18		Very thin	4881
19		Very thin	4887
20	FeI	Thin	4920
21	(HeI, LaI)	Medium dense	4922
22	TiI	Thin	4928
23	FeI(double)	Thin	4952
24	FeI(double)	Thin	5012
25	(FeI, HeI)	Medium dense	5015
	HeI	Thinnest	5048
26	MgI(b_4)	Medium dense	5167
27	MgI(b_2)	Dense	5173
28	MgI(b_1)	Dense	5183
29		Thinnest	5188
30		Thin	5205
31		Thin	5208
32		Thin	5227
33		Thinnest	5234
34		Thin	5271
35		Thinnest	5276
36	FeXIV	Thinnest	5303
37		Thin	5318
38		Very thin	5328
39		Very thin	5337
40		Thin	5494
41	HeI(D_3)	Densest	5876
42	NaI(D_2)	Dense	5890
43	NaI(D_1)	Dense	5896
44	[a]BaII	Medium dense	6142
45	[a]CaI	Very thin	6162
46	FeX	Very thin	6374
47	(CaI, FeI, BaII)	Very thin	6494-6497
48	HI(H_α)	Densest	6563
49	HeI	Medium dense	6678

[a]indicates only tentative identification

TABLE IV.- CORRECTION FOR INSTRUMENTAL AND SKY BACKGROUNDS

$$\left\{ 3050 \left[\frac{N_s(r)}{N_{IM}(1.25\ R_\odot)} \right]_{\substack{\text{lens} \\ \text{window} \\ \text{filter}}} + 4_{sky} \right\} 10^{-10}\ B_\odot$$

$r/R_\odot$	Total correction (units of $10^{-10}\ B_\odot$)	$r/R_\odot$	Total correction (units of $10^{-10}\ B_\odot$)
1.20	50^x	2.3	9
1.25	40^x	2.4	8
1.30	34^x	2.6	7.5
1.35	30^x	2.8	7
1.40	26^x	3.0	6.5
1.45	23^x	3.5	5.5
1.50	21^x	4.0	5.0
1.6	18	4.5	4.7
1.7	15	5.0	4.5
1.8	13.5	5.5	4.4
1.9	12	6.0	4.3
2.0	11	6.5	4.2^x
2.1	10	7.0	4.2^x
2.2	9.5	8.0	4.1^x

(x indicates the value of scattering extrapolated from measured region)

Figure 1.- Camera installation.

A-34471
Sta. 7-16

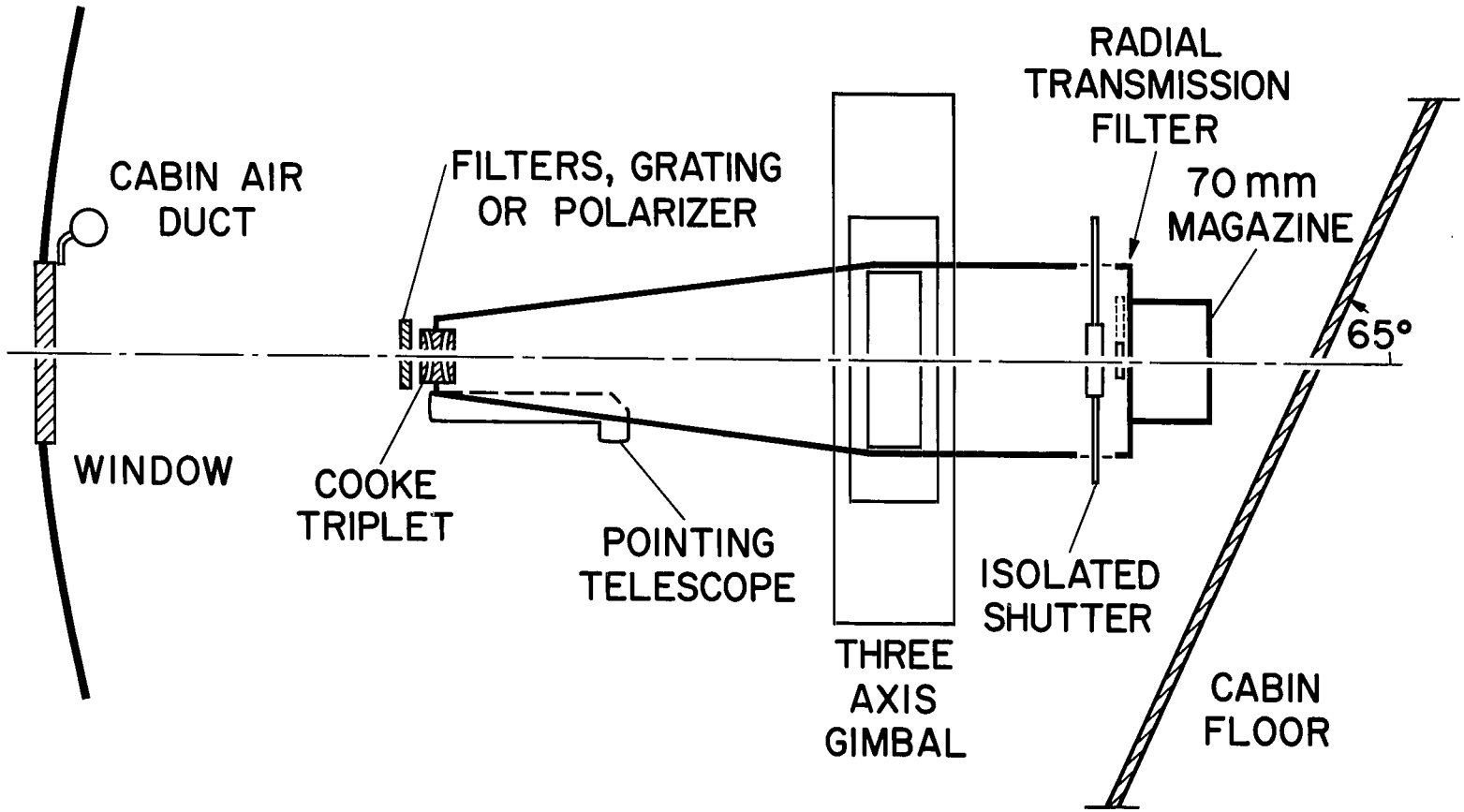

Figure 2.- Schematic drawing of camera.

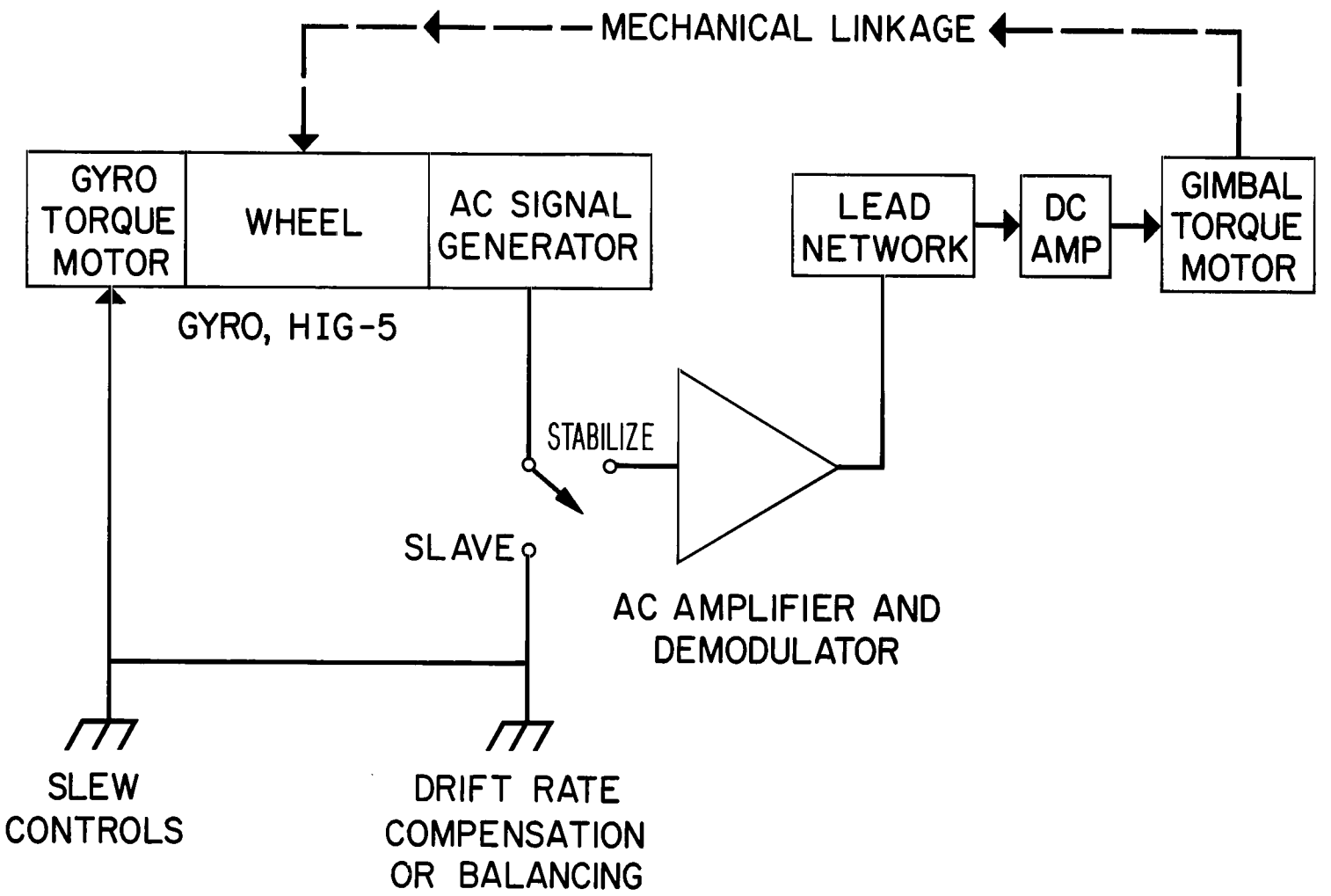

Figure 3.- Stabilization system (closed loop, inertial stabilization of one-gimbal axis).

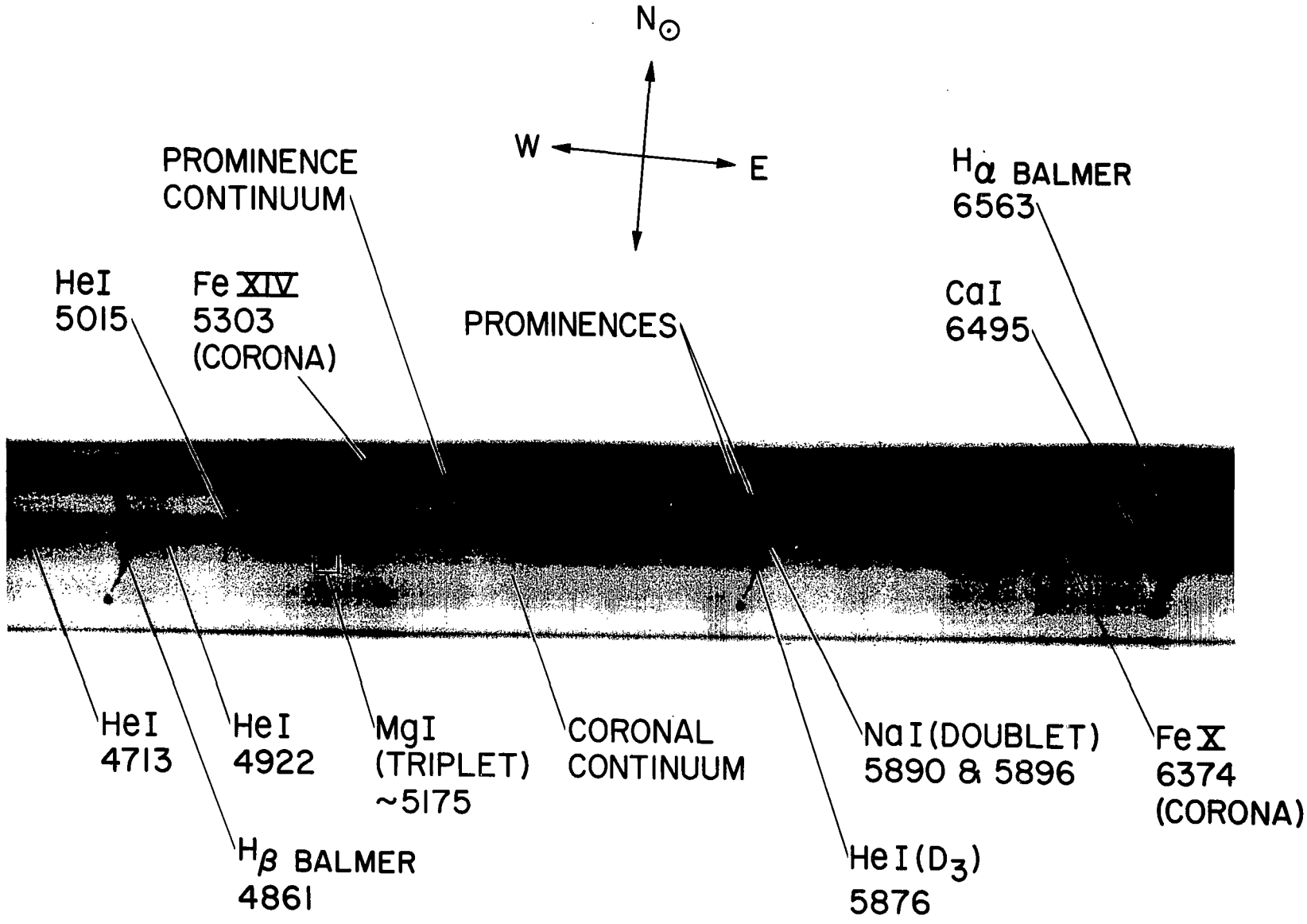

Figure 4.- Flash spectrum.

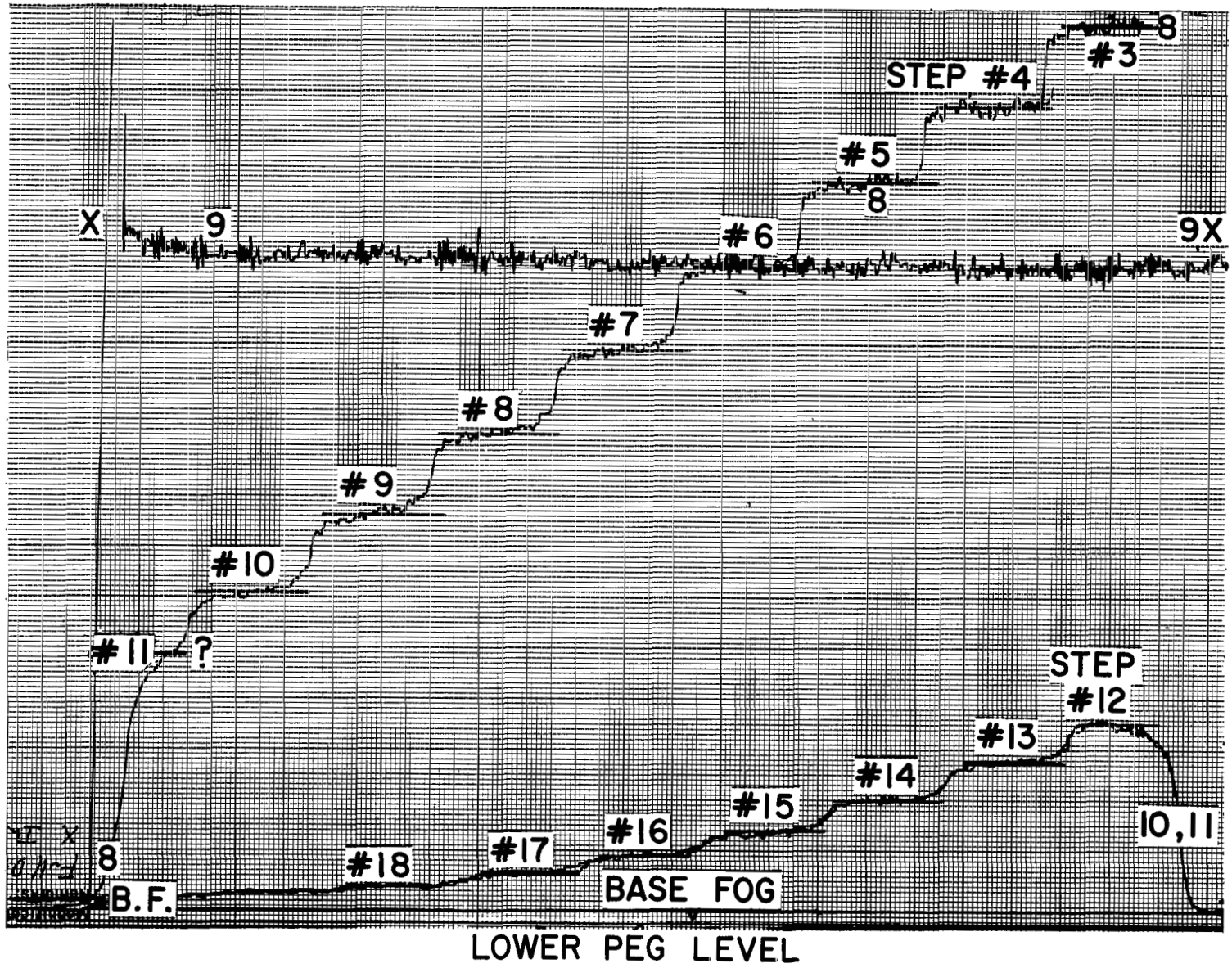

Figure 5.- Microdensitometry of calibration frame 14 (records 7a, b, c, and d of frame 14).

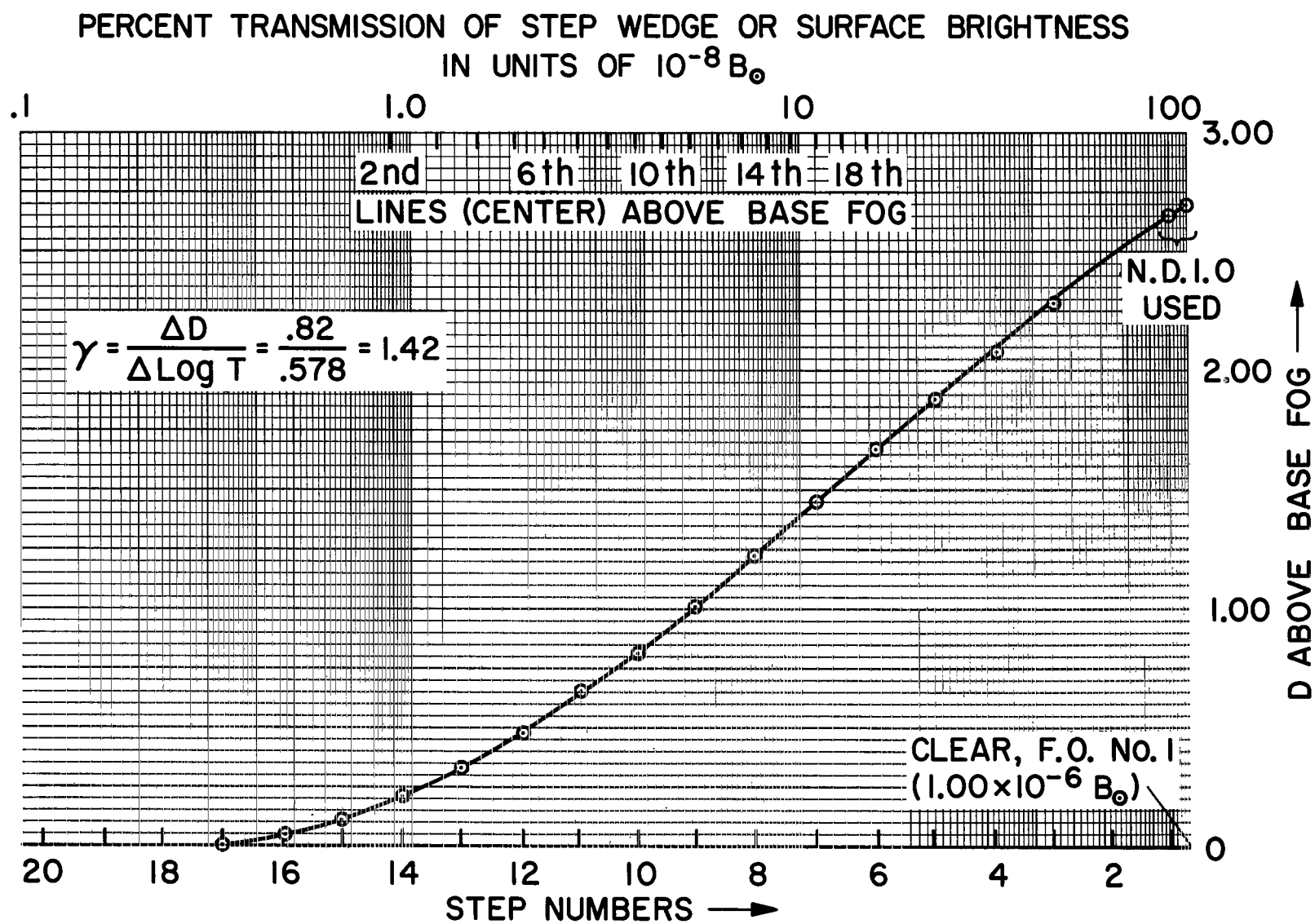

Figure 6.- Characteristic curve (records 7a, b, c, and d of frames 4 and 14, 0.2-second exposure).

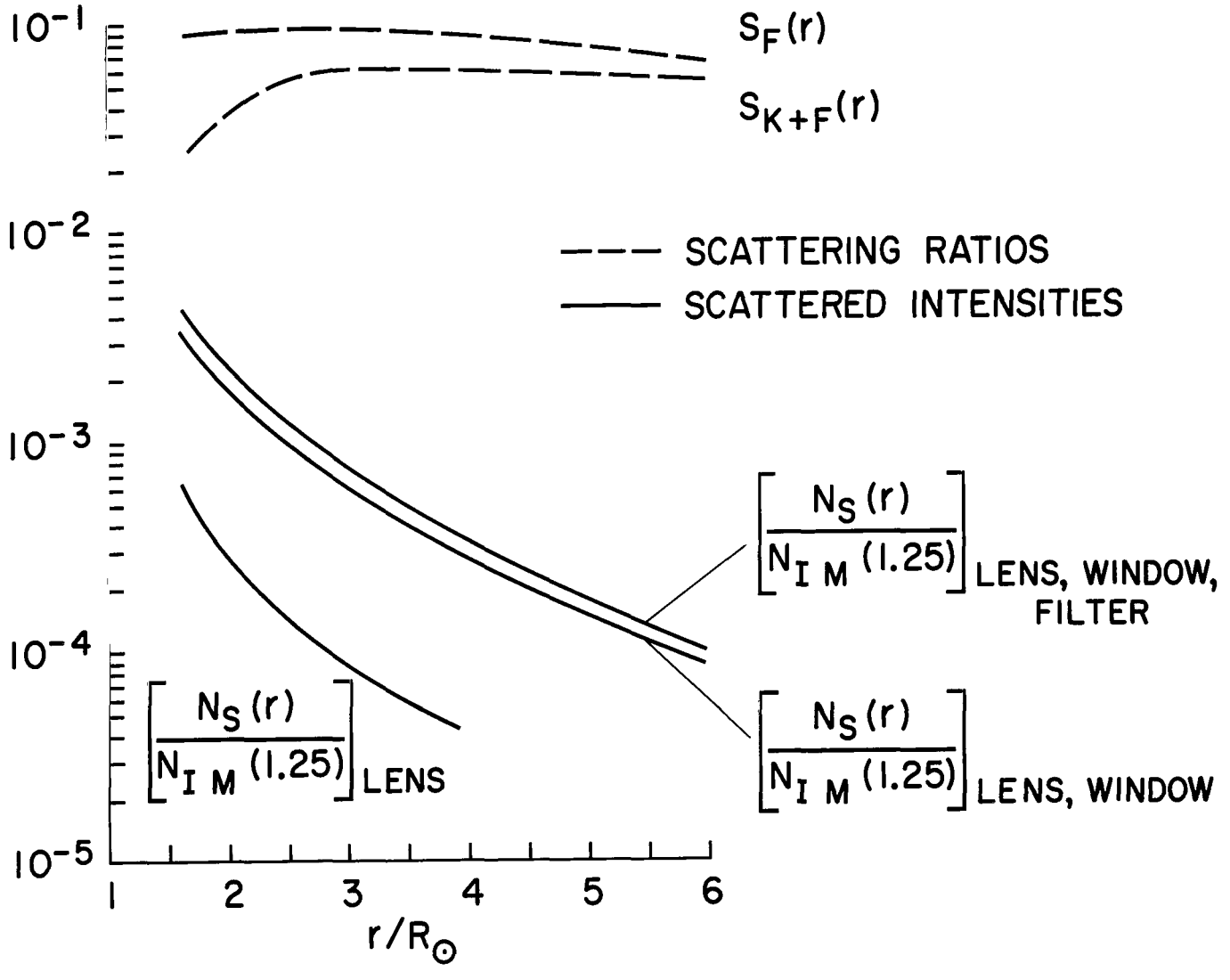

Figure 7.- Scattering curves.

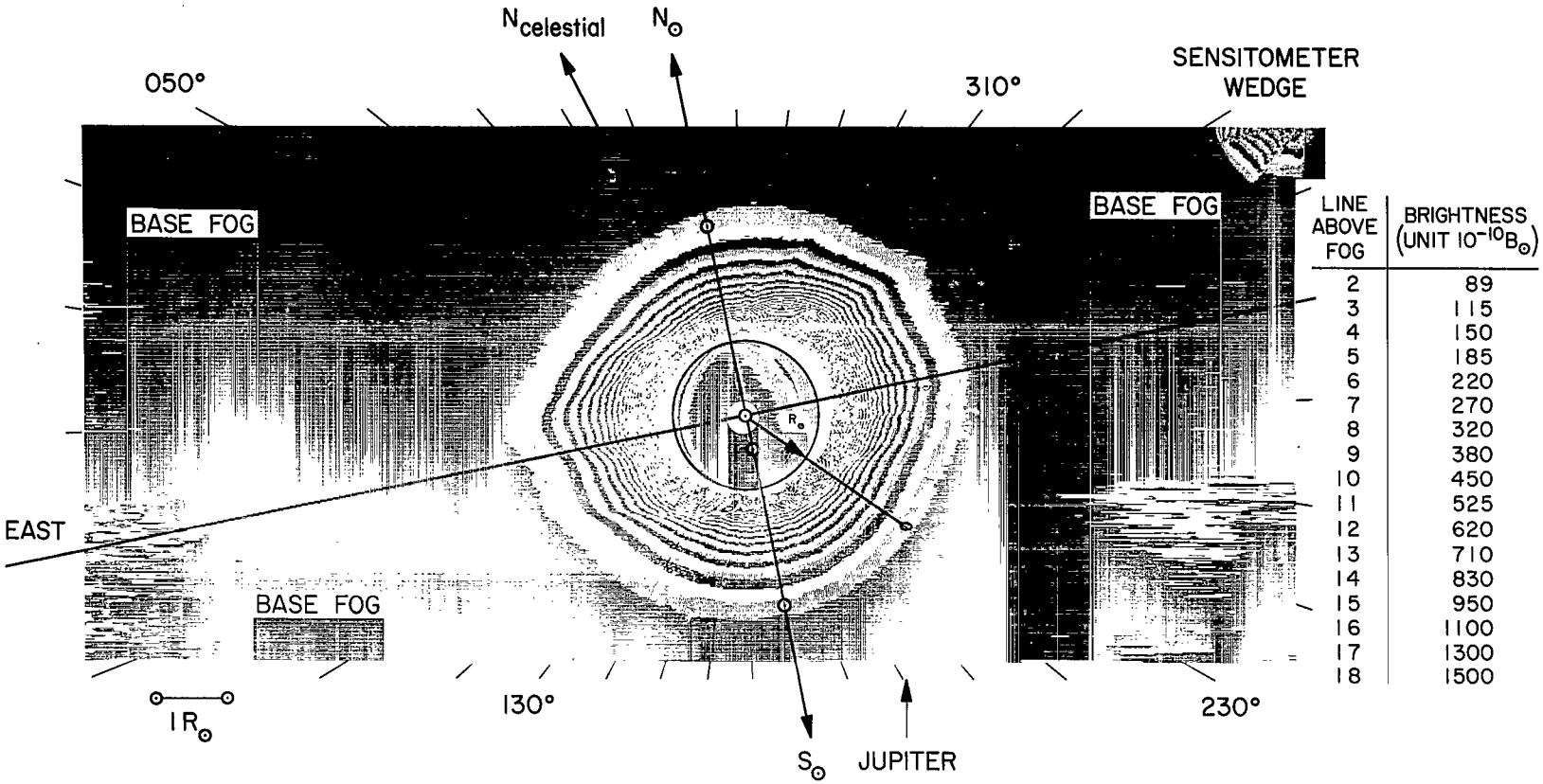

Figure 8.- Inner coronal isophotes.

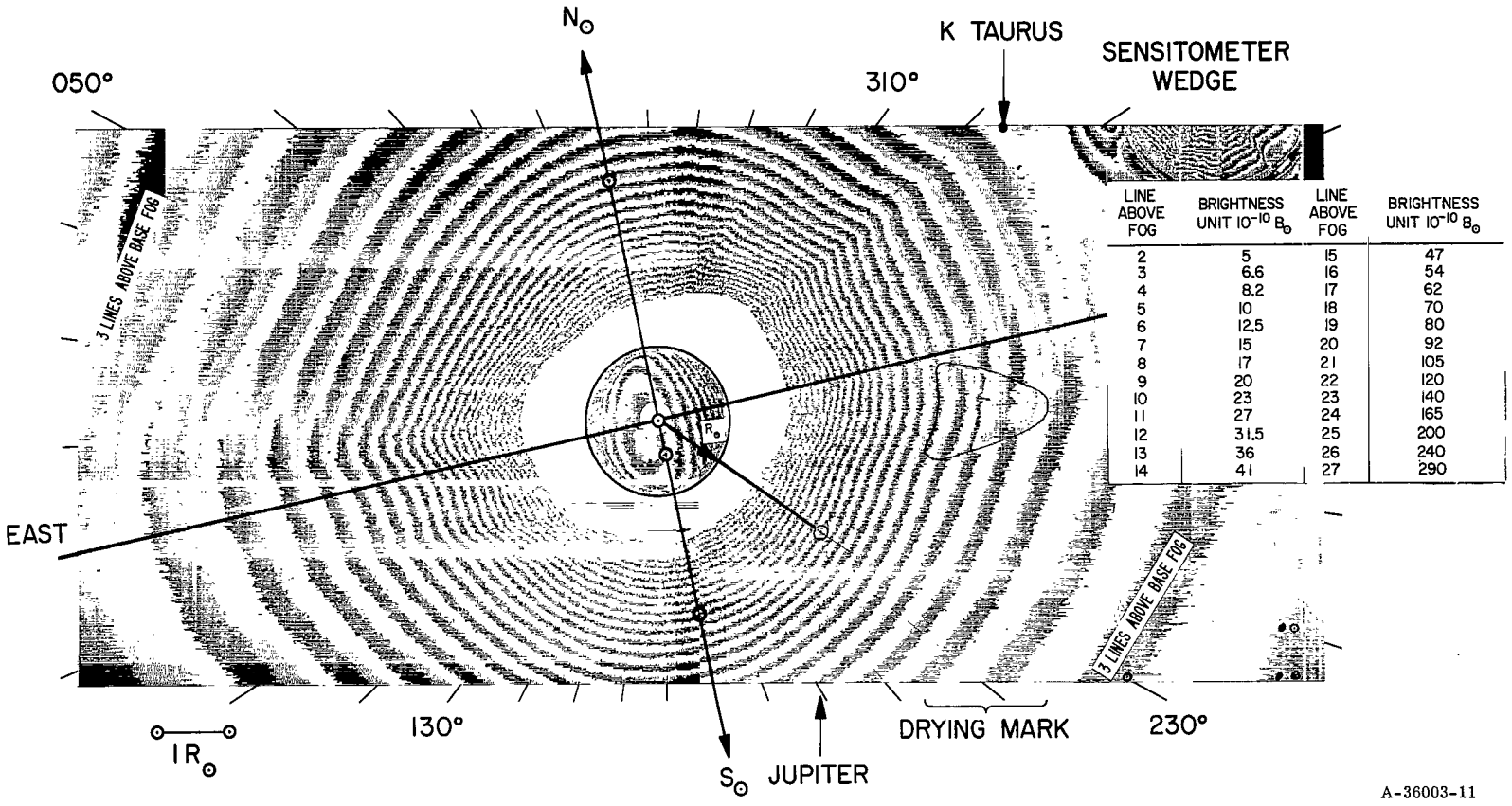

LINE ABOVE FOG	BRIGHTNESS UNIT 10^{-10} $B_\odot$	LINE ABOVE FOG	BRIGHTNESS UNIT 10^{-10} $B_\odot$
2	5	15	47
3	6.6	16	54
4	8.2	17	62
5	10	18	70
6	12.5	19	80
7	15	20	92
8	17	21	105
9	20	22	120
10	23	23	140
11	27	24	165
12	31.5	25	200
13	36	26	240
14	41	27	290

Figure 9.- Outer coronal isophotes.

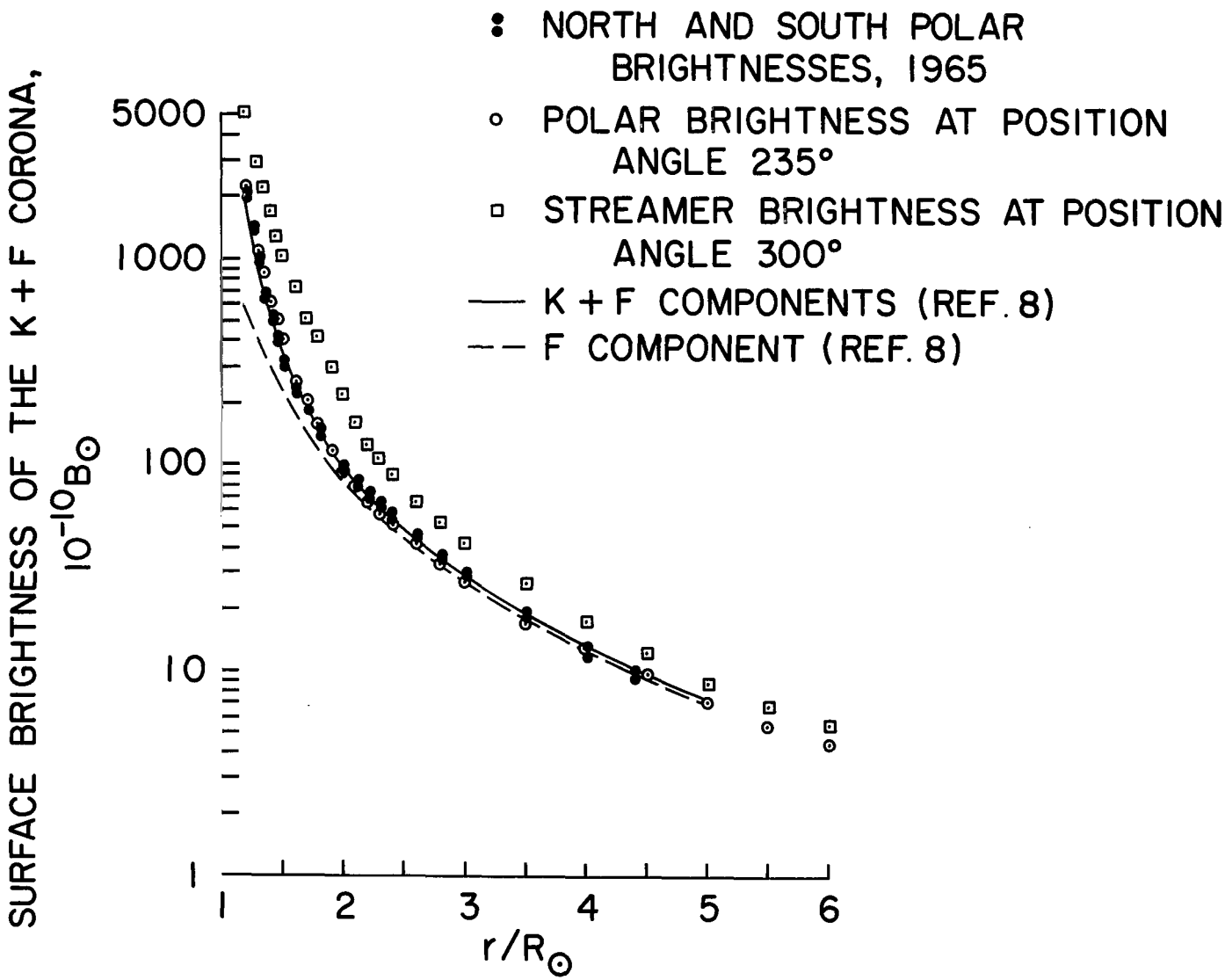

Figure 10.- Coronal brightness.

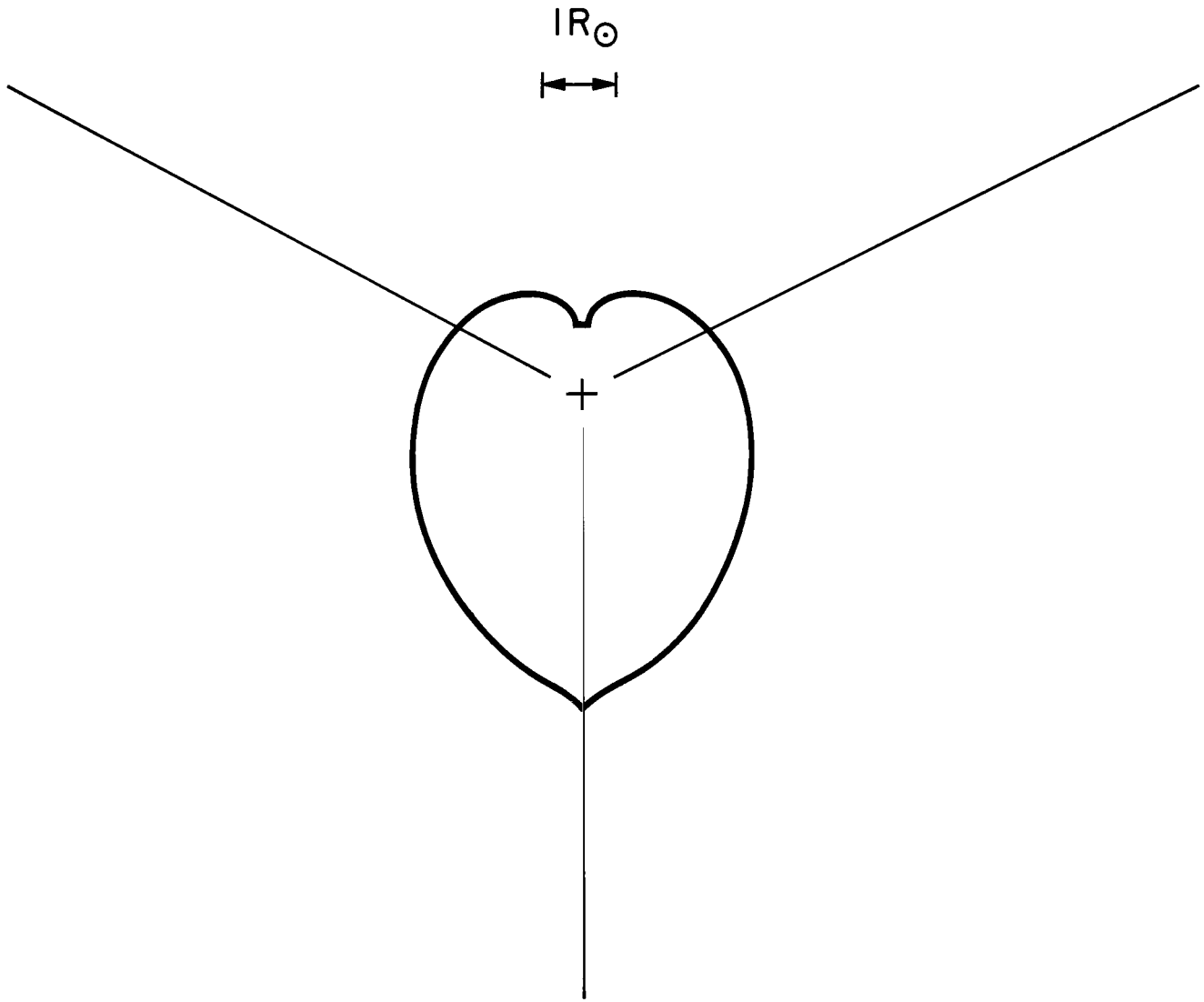

Figure 11.- Radial transmission filter occulting disk with support wires.

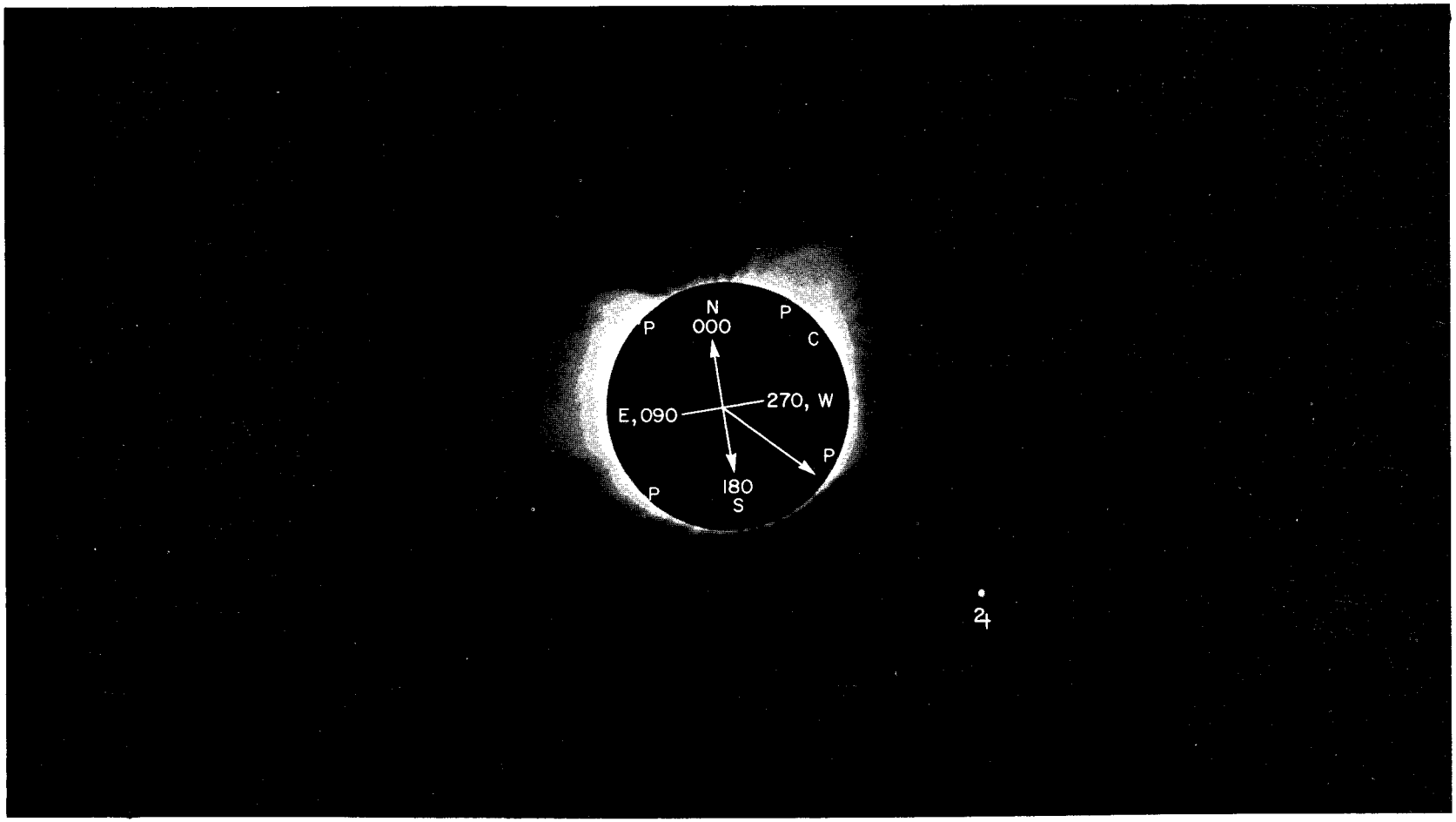

Figure 12.- Inner corona (fourth generation print of 0.5-second exposure).

A-34471-160

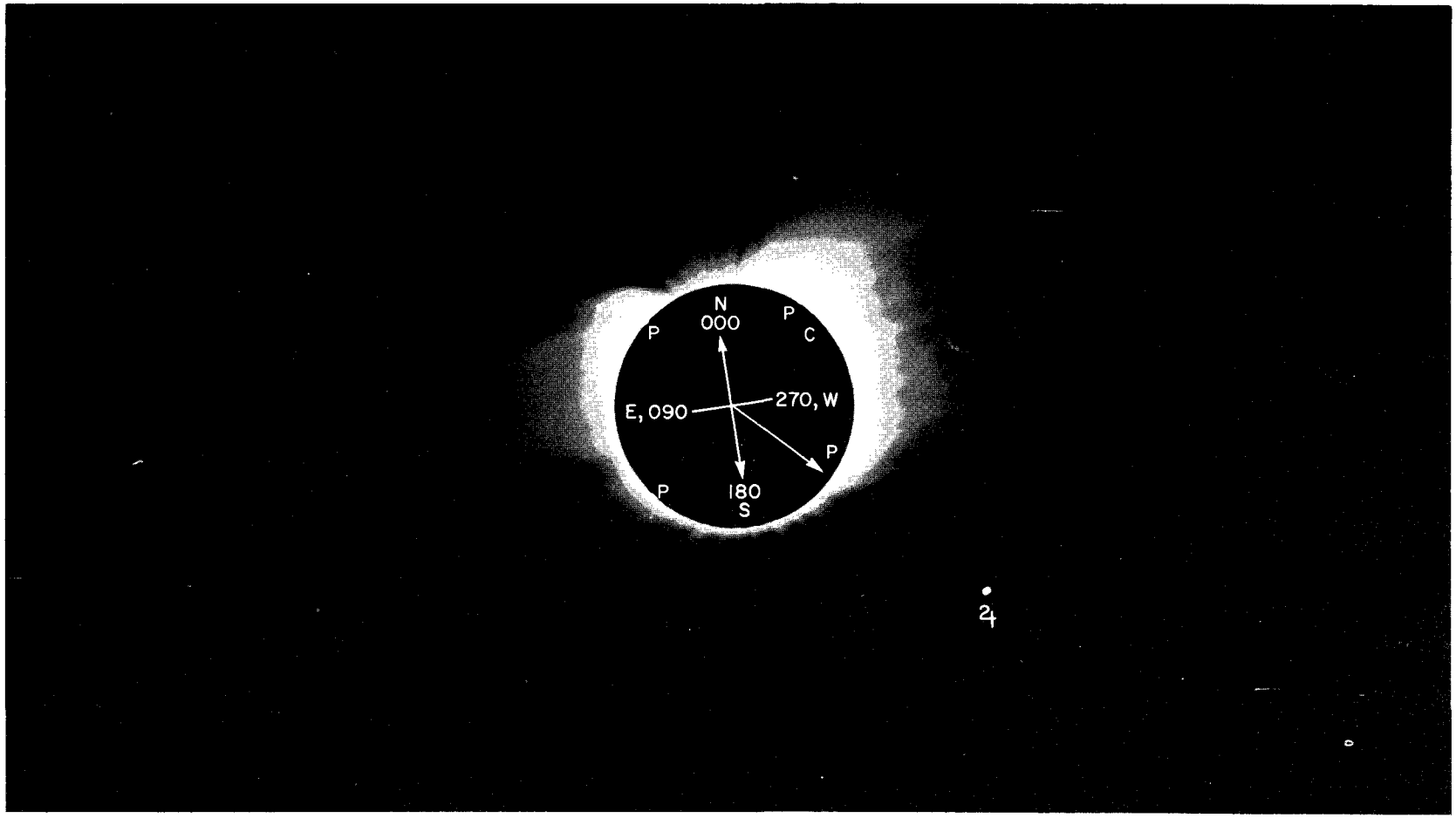

Figure 13.- Midcorona (fourth generation print of 1-second exposure).

A-34471-161

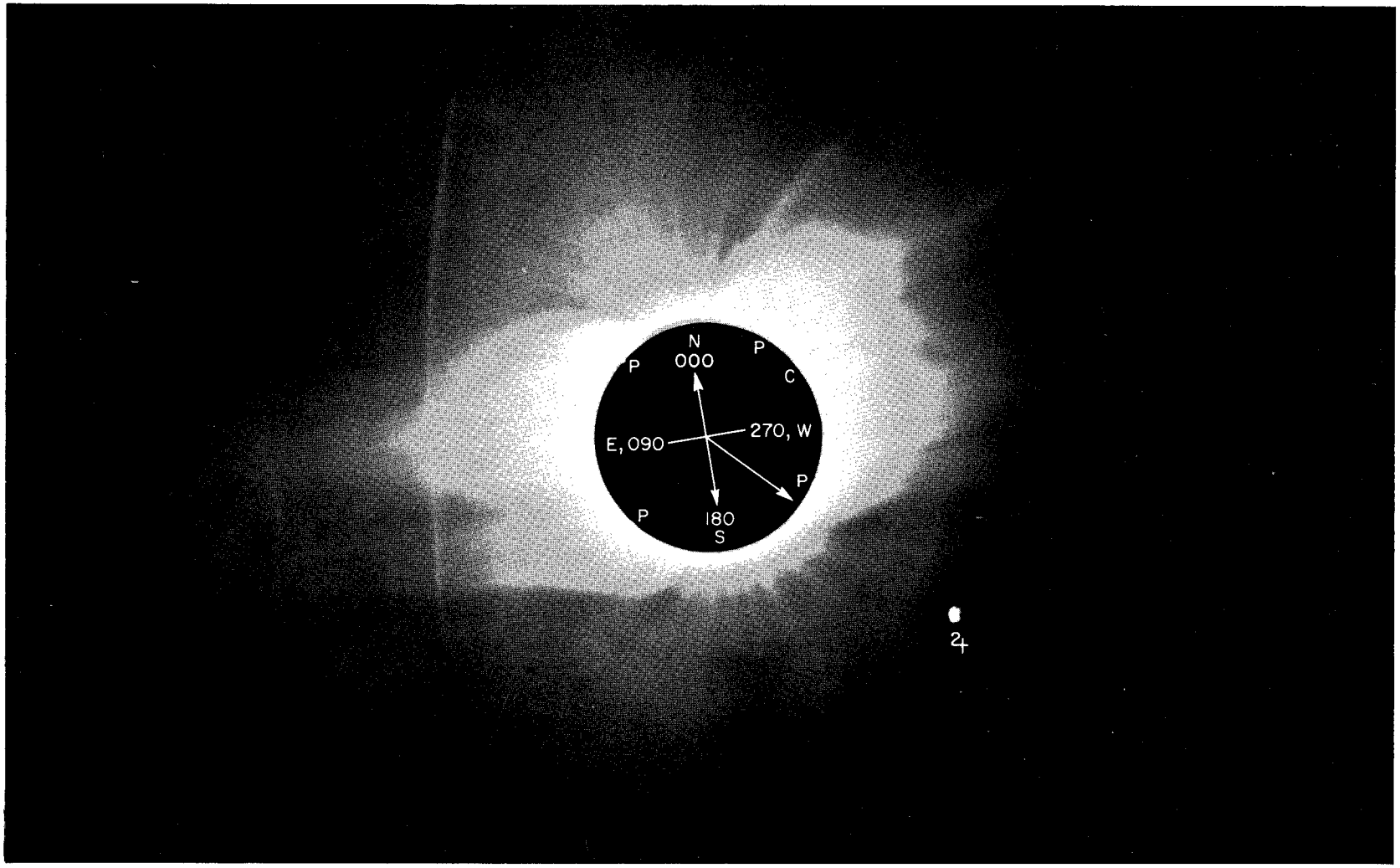

Figure 14.- Outer corona (fourth generation print of 5-second exposure).

A-34471-159

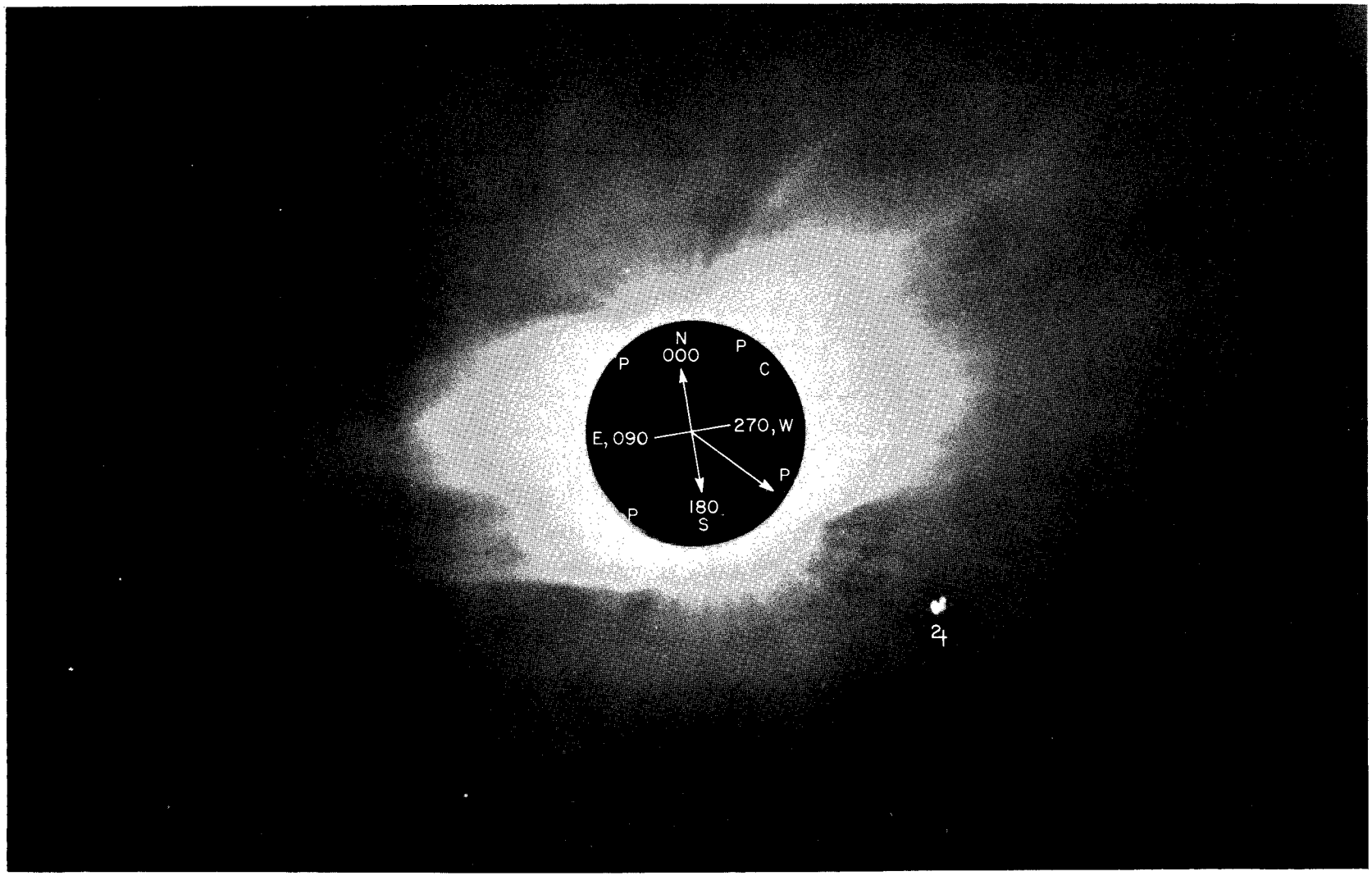

Figure 15.- Outer corona (fourth generation print of 10-second exposure).

A-34771-158

"The aeronautical and space activities of the United States shall be conducted so as to contribute . . . to the expansion of human knowledge of phenomena in the atmosphere and space. The Administration shall provide for the widest practicable and appropriate dissemination of information concerning its activities and the results thereof."

—NATIONAL AERONAUTICS AND SPACE ACT OF 1958

NASA SCIENTIFIC AND TECHNICAL PUBLICATIONS

TECHNICAL REPORTS: Scientific and technical information considered important, complete, and a lasting contribution to existing knowledge.

TECHNICAL NOTES: Information less broad in scope but nevertheless of importance as a contribution to existing knowledge.

TECHNICAL MEMORANDUMS: Information receiving limited distribution because of preliminary data, security classification, or other reasons.

CONTRACTOR REPORTS: Scientific and technical information generated under a NASA contract or grant and considered an important contribution to existing knowledge.

TECHNICAL TRANSLATIONS: Information published in a foreign language considered to merit NASA distribution in English.

SPECIAL PUBLICATIONS: Information derived from or of value to NASA activities. Publications include conference proceedings, monographs, data compilations, handbooks, sourcebooks, and special bibliographies.

TECHNOLOGY UTILIZATION PUBLICATIONS: Information on technology used by NASA that may be of particular interest in commercial and other non-aerospace applications. Publications include Tech Briefs, Technology Utilization Reports and Notes, and Technology Surveys.

Details on the availability of these publications may be obtained from:

SCIENTIFIC AND TECHNICAL INFORMATION DIVISION

NATIONAL AERONAUTICS AND SPACE ADMINISTRATION

Washington, D.C. 20546